Chapter 3:

UV Emission and Energy Transfer Process in

xCe^{3+}, yGd^{3+}: $La_{2-(x+y)}O_3$

&

xPr^{3+}, yGd^{3+}: $La_{2-(x+y)}O_3$

Phosphors

Abstract:

Despite being a harmful radiation, there are many useful applications of UV radiation. This includes its use in the biomedical field. Hence, it is required to generate the UV radiation with desired characteristics. There are many compounds based on a combination of rare earth elements like Ce, Gd, Pr, which serve as UV emitting phosphors. In this work, seven rare earth based compounds i. e. 1% Ce^{3+}: La_2O_3, 1% Gd^{3+}: La_2O_3, 1% Ce^{3+} - 1% Gd^{3+}: La_2O_3, 2% Ce^{3+} - 1% Gd^{3+}: La_2O_3, 1% Pr^{3+}: La_2O_3, 1% Pr^{3+} - 1% Gd^{3+}: La_2O_3, and 2% Pr^{3+} - 1% Gd^{3+}: La_2O_3 have been synthesized to study their UV emission properties and understand the energy transfer process there in. The XRD & EDAX analysis reveals that the obtained compounds possess high purity and are in hexagonal phase with crystallite size in nanometer. The bandgap and refractive index have been calculated from absorption spectra obtained from UV – Visible spectrometer. The emission of 1% Gd^{3+}: La_2O_3 falls in UVB region while for 1% Ce^{3+}: La_2O_3 & 1% Pr^{3+}: La_2O_3, it is in UVA region. Both, UVA and UVB emission has been recorded in 1% Ce^{3+} - 1% Gd^{3+}: La_2O_3, 2% Ce^{3+} - 1% Gd^{3+}: La_2O_3. In 1% Pr^{3+} - 1% Gd^{3+}: La_2O_3 and 2% Pr^{3+} - 1% Gd^{3+}: La_2O_3, the emission has been recorded in the visible region with high quantum efficiency due to the energy transfer from Gd^{3+} ion to Pr^{3+} ion and thus has the potential to serve as LED phosphor of cyan color. The parameters like redshift D, centroid shift ε_c and crystal field splitting ε_{cfs} have been calculated for Ce & Ce – Gd based La_2O_3 compounds. Compared with previously reported UV emitting phosphors, the compounds synthesized for this work have less complexity in terms of chemical composition and structure. The synthesis process is also relatively simple and eco-friendly with fewer elements used and giving higher yield of products.

Keywords: UV emission, XRD analysis, EDAX spectra, UV – Visible analysis, PL analysis

Graphical Abstract:

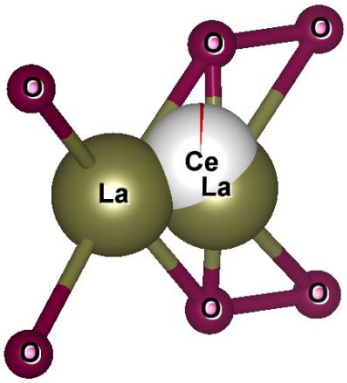

xCe^{3+}: $La_{2-x}O_3$

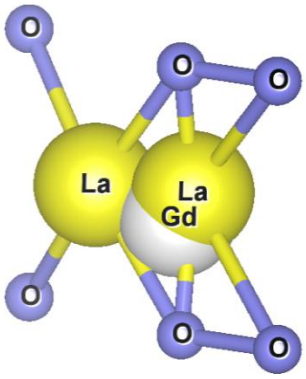

xGd^{3+}: $La_{2-x}O_3$

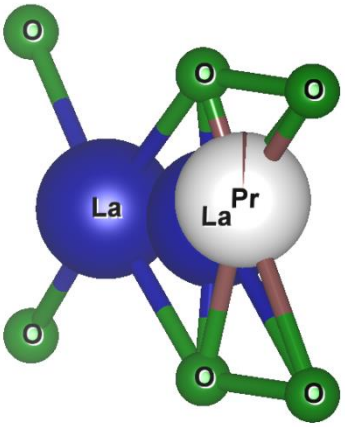

xPr^{3+}: $La_{2-x}O_3$

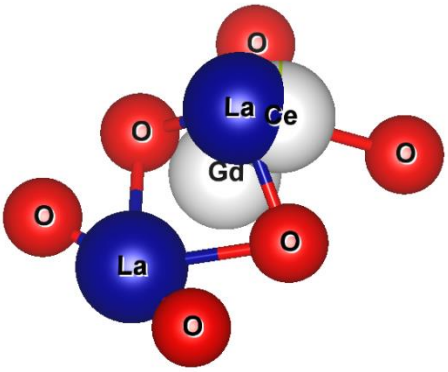

xCe^{3+}, yGd^{3+}: $La_{2-(x+y)}O_3$

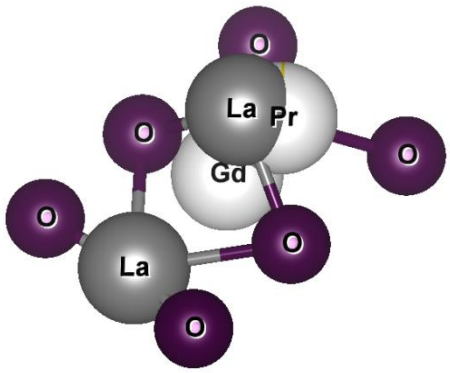

xPr^{3+}, yGd^{3+}: $La_{2-(x+y)}O_3$

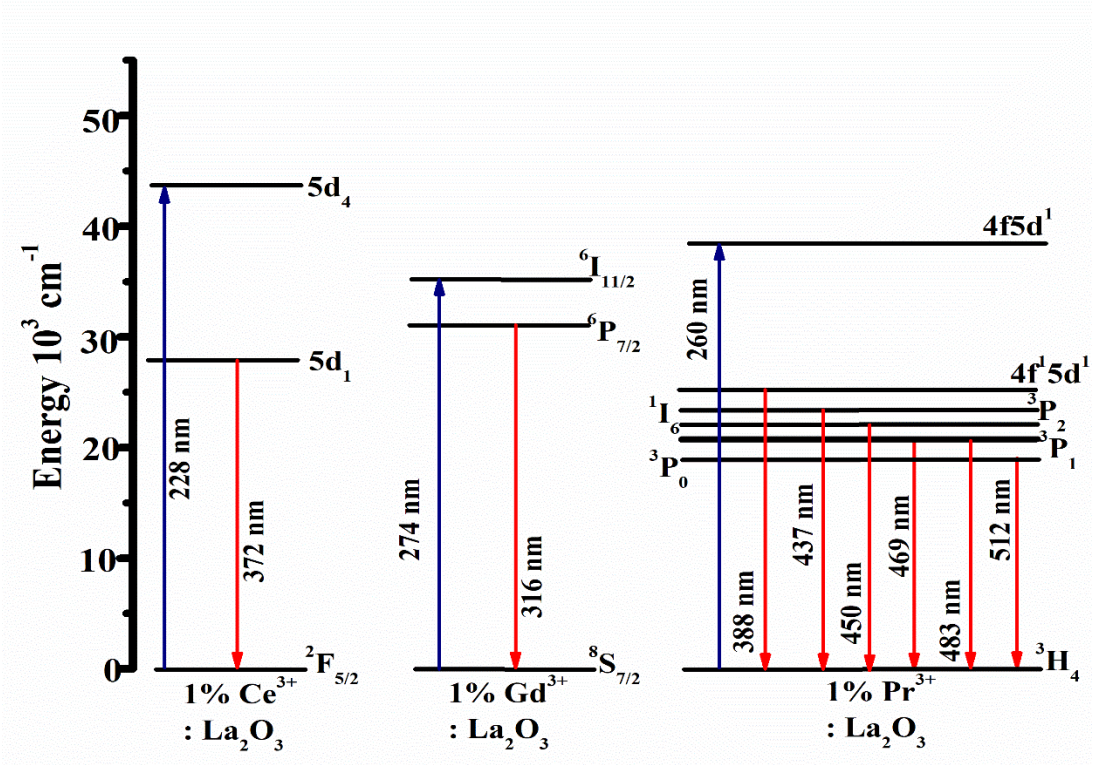
Energy 10^3 cm^{-1}
50
40
30
20
10
0
$5d_4$
$5d_1$
$^2F_{5/2}$
228 nm
372 nm
1% Ce^{3+}
: La_2O_3
$^6I_{11/2}$
$^6P_{7/2}$
$^8S_{7/2}$
274 nm
316 nm
1% Gd^{3+}
: La_2O_3
$4f5d^1$
$4f^15d^1$
$^1I_6$
$^3P_2$
$^3P_1$
$^3P_0$
$^3H_4$
260 nm
388 nm
437 nm
450 nm
469 nm
483 nm
512 nm
1% Pr^{3+}
: La_2O_3

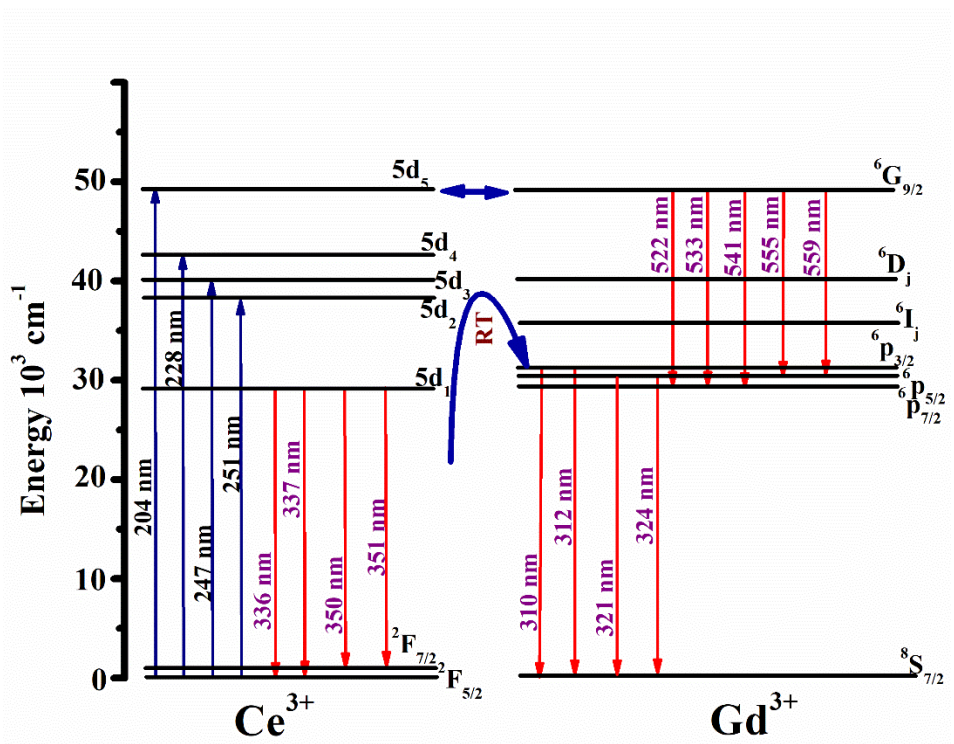
Energy 10^3 cm^{-1}
50
40
30
20
10
0
$5d_5$
$5d_4$
$5d_3$
$5d_2$
$5d_1$
$^2F_{7/2}$
$^2F_{5/2}$
204 nm
228 nm
247 nm
251 nm
336 nm
337 nm
350 nm
351 nm
RT
$^6G_{9/2}$
^6D_j
^6I_j
$^6p_{3/2}$
$^6p_{5/2}$
$^6p_{7/2}$
$^8S_{7/2}$
522 nm
533 nm
541 nm
555 nm
559 nm
310 nm
312 nm
321 nm
324 nm
Ce^{3+}
Gd^{3+}

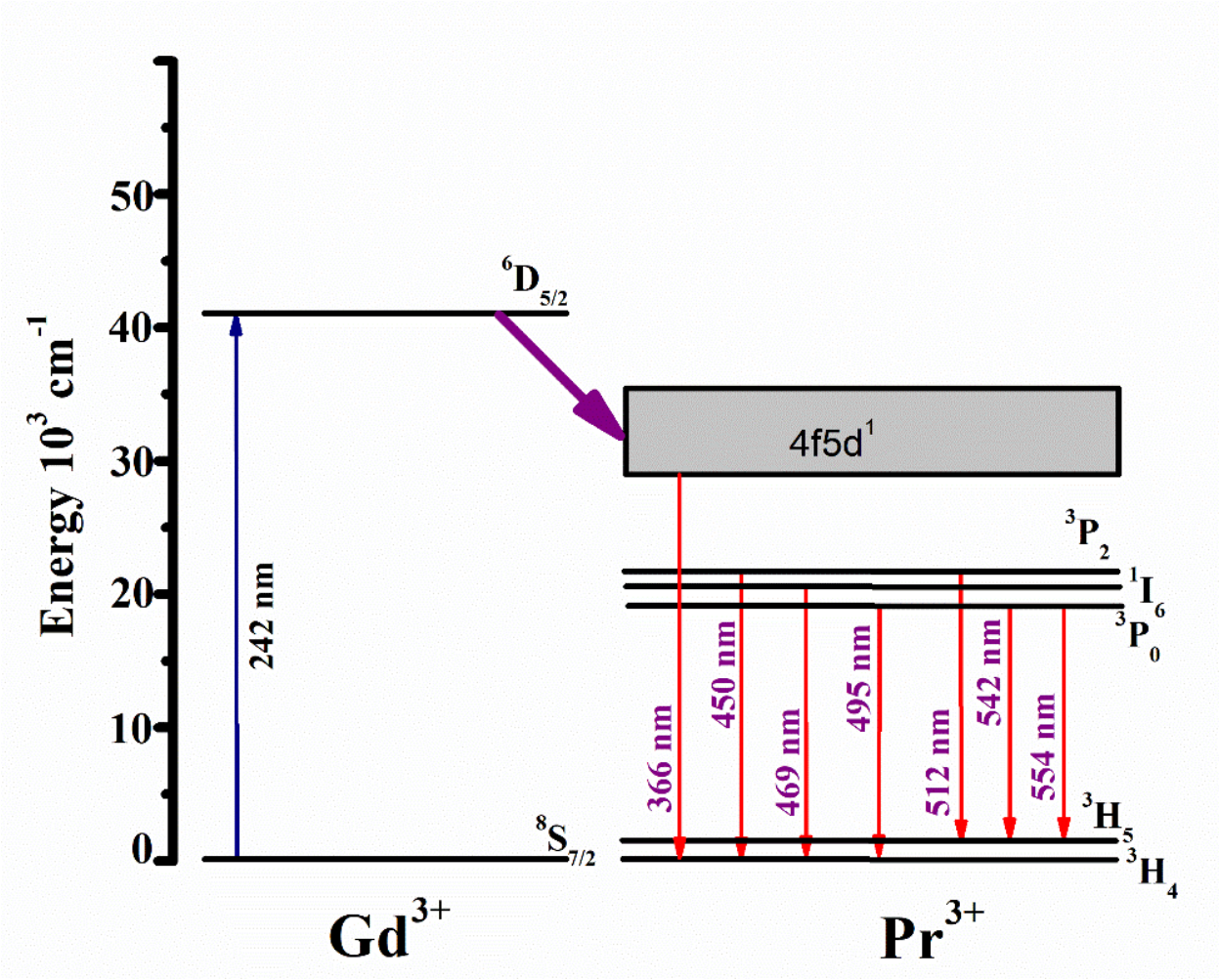

3.1 Introduction:

To begin with an old idiom which translates as "What kills is harmful but can be beneficial and at times nourishing as well"; this applies to UV radiation. The UV radiation is very harmful but it has useful applications in several fields. One of the most prominent applications is in the biomedical field that is very helpful for humankind. Currently, UV radiation-based treatment has shown the potency to be one of the effective preventive measures for COVID 19 [1].

The UV radiation is categorized into three sections according their wavelength. These are UVA

(400 nm – 320 nm), UVB (320 nm – 280 nm) & UVC (280 nm – 100 nm). Each range has different applications. UVA & UVB radiation are useful in phototherapy treatment of skin diseases like Psoriasis [2], Eczema [3], Jaundice [3][4], Vitiligo [5], Atopic dermatitis [6] and Scleroderma [7]. The UVA radiation has application in sewage water treatment plant [8], bug zapper [9], white light LED [10] and photocopying. The UVB radiation is helpful to produce Vitamin D in the body [11]. UVC radiation emitting phosphors are used in germicidal lamps that are effective in the decontamination of surfaces and water [12]. These extensive applications of UV radiation attract many researchers and manufacturers to do research in the field of UV emitting phosphors.

There are many compounds based on the rare earth elements like Cerium(Ce), Gadolinium(Gd) & Praseodymium(Pr) that are very good candidates for UV emitting phosphors. Moreover, their combinations as sensitizer-activator can also be used as UV emitting phosphors. The 5d4f energy level transition in Ce, Pr elements and higher 4f energy levels in Gd enable them to emit UV radiation [13] [14]. There are many Ce^{3+} based phosphors like Ce^{3+}: $Ba_2GaB_4O_9Cl$ [15], Ce^{3+}: $Ca_2YHF_2Ga_2O_{12}$ [16], Ce^{3+}: $LiYP_4O_{12}$ [17], Ce^{3+}: $LiYF_4$ [18], Ce^{3+}: $CaSO_4$ [18], Ce^{3+}: YPO_4 [18], Ce^{3+}: $ScPO_4$ [18] and others with Gd as co – dopant like (Gd, Ce): SrF_2 [19], Ce^{3+}: $KGd(PO_3)_4$ [20], Li(Y, Gd)F_4: Ce^{3+} [21], $Gd_2(SiO_4)$ O: Ce^{3+} [22], Gd^{3+}, Ce^{3+}: $KZnSO_4Cl$ [23], YAG: Ce^{3+}, Gd^{3+} [24], which emit UV radiation.

The UV emission wavelength of any Ce^{3+} and Ce^{3+} - Gd^{3+} based phosphors is dependent on host environment. The parameter like Redshift D, Centroid shift ε_c and Crystal field splitting ε_{cfs} of Ce elements are greatly affected by host compounds [18]. The Gd^{3+} based compounds like Gd^{3+}: $LiBaB_9O_{15}$ [25], Gd^{3+}: $LaPO_4$ [26], $(Sr, Gd)_9Mg_{1.5}(PO_4)_7$ [27], Gd^{3+}: $LiSrBO_3$ [28], Gd based Phosphate glass [29], Gd^{3+}: $LaBiB_2O_3$ [30], Na(Y, Gd)F PO_4 [31] and Gd^{3+}: BaB_9O_{16} [32] have

been previously reported as UV emitting phosphors. The Pr^{3+} and Pr^{3+} & Gd^{3+} (as dopant) combination based compound such as Pr^{3+}: La $(OH)_3/La_2O_3$ [33], Gd^{3+} - Pr^{3+}: RMO_3(R = Y, La; M = Al, Ga) [34], Pr^{3+}: $ScBO_3$ [35], Pr^{3+}: ZnO_2 [36], Pr^{3+}: $K_3Lu_{1-x}Y_x(PO_4)_2$ [37], Pr^{3+}: $Y_3Al_{5-x}Ga_xO_{12}$ [38] are also reported UV emitting phosphors.

In this work, seven samples 1% Ce^{3+}: La_2O_3, 1% Gd^{3+}: La_2O_3, 1% Ce^{3+} - 1% Gd^{3+}: La_2O_3, 2% Ce^{3+} - 1% Gd^{3+}: La_2O_3, 1% Pr^{3+}: La_2O_3, 1% Pr^{3+} - 1% Gd^{3+}: La_2O_3, and 2% Pr^{3+} - 1% Gd^{3+}: La_2O_3 have been synthesized by using Solid-State method. The primary aim is to study the UV emission characteristics and associated energy transfer process. Among these, four samples i. e. 1% Ce^{3+}: La_2O_3, 1% Gd^{3+}: La_2O_3, 1% Ce^{3+} - 1% Gd^{3+}: La_2O_3 & 2% Ce^{3+} - 1% Gd^{3+}: La_2O_3 show emission only in the UV region, while the Pr – Gd based La_2O_3 compounds give emission in the visible region also, although with seemingly higher efficiency. One of the intense emission peak in the visible region being of cyan color opens the prospects of the material to be used as LED phosphor.

As mentioned above, the synthesis process fares better compared to the previously reported methods for synthesis of UV emitting phosphors because the material prepared has less complexity in compositional and structural aspects. The synthesis process is simple, uses less number of ingredients, is environment friendly and gives better yield with the material being nano crystalline in nature. The process would be industry friendly as well.

The UV emission properties & energy transfer process of 1% Ce^{3+}: La_2O_3, 1% Gd^{3+}: La_2O_3, 1% Ce^{3+} - 1% Gd^{3+}: La_2O_3, 2% Ce^{3+} - 1% Gd^{3+}: La_2O_3 compounds and the co-activated 1% Pr^{3+} - 1% Gd^{3+}: La_2O_3, and 2% Pr^{3+} - 1% Gd^{3+}: La_2O_3 compounds have been presented for the first time in this work. arameters like Redshift D, Centroid shift ε_c and Crystal field splitting ε_{cfs} of

Ce and Ce – Gd based La_2O_3 compounds have been also calculated for the first time.

3.2 Experimental Procedure:

As mentioned above, the samples (1% Ce^{3+}: La_2O_3, 1% Gd^{3+}: La_2O_3, 1% Pr^{3+}: La_2O_3, 1% Ce^{3+}, 1% Gd^{3+}: La_2O_3, 2% Ce^{3+}, 1% Gd^{3+}: La_2O_3, 1% Pr^{3+}, 1% Gd^{3+}: La_2O_3 & 2% Pr^{3+}, 1% Gd^{3+}: La_2O_3) were synthesized by Solid State technique.

For the sample-1 i. e. 1% Ce: La_2O_3, the precursors $Ce(NO_3)_3{\cdot}6H_2O$ & $La(NO_3)_3{\cdot}6H_2O$ were taken in stoichiometric ratio and dissolved in 5 ml De-Ionized (DI) water. This mixture was poured in a alumina crucible and kept in a furnace at 1100°c for 4 hours. Then the crucible was allowed to get cooled at room temperature. The obtained material which was porous in nature was then crushed with the help of mortal and pastel into powder form. The other six compounds were synthesized in a similar manner with different doping elements and doping percentage.

The XRD, EDAX, UV – Visible & Photoluminescence studies were carried out for all synthesized samples to analyze their structural, elemental and optical properties.

3.3 Results and Analysis:

3.3.1 Structural and elemental analysis:

A Rigaku SmartLab diffractometer operating at 30 mA & 40 kV was used for XRD characterization. Cu K_α radiation was used in the 2θ scan range of 10° to 90°, with a step of 0.02°.

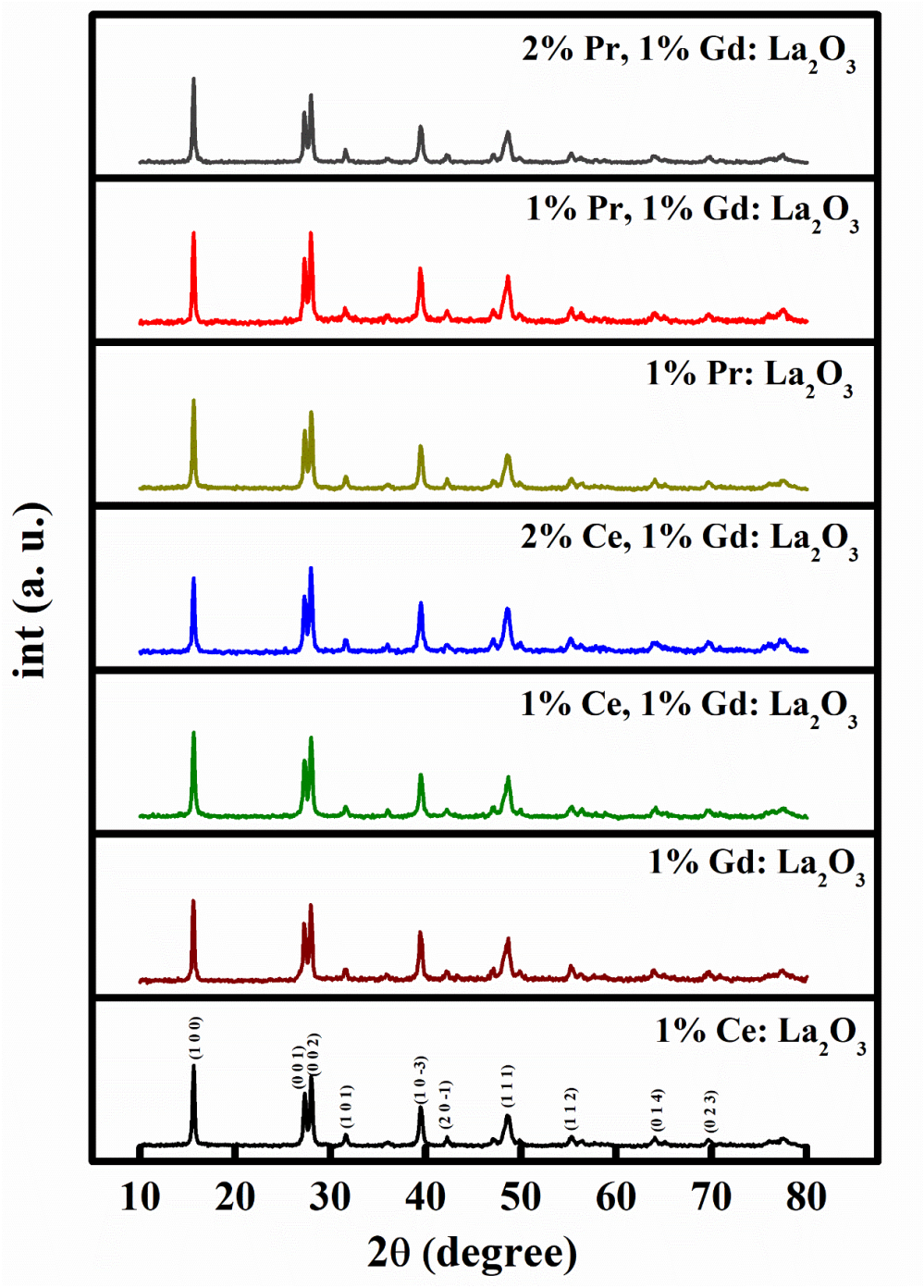

Figure 3.1 XRD Spectra of Synthesized Samples

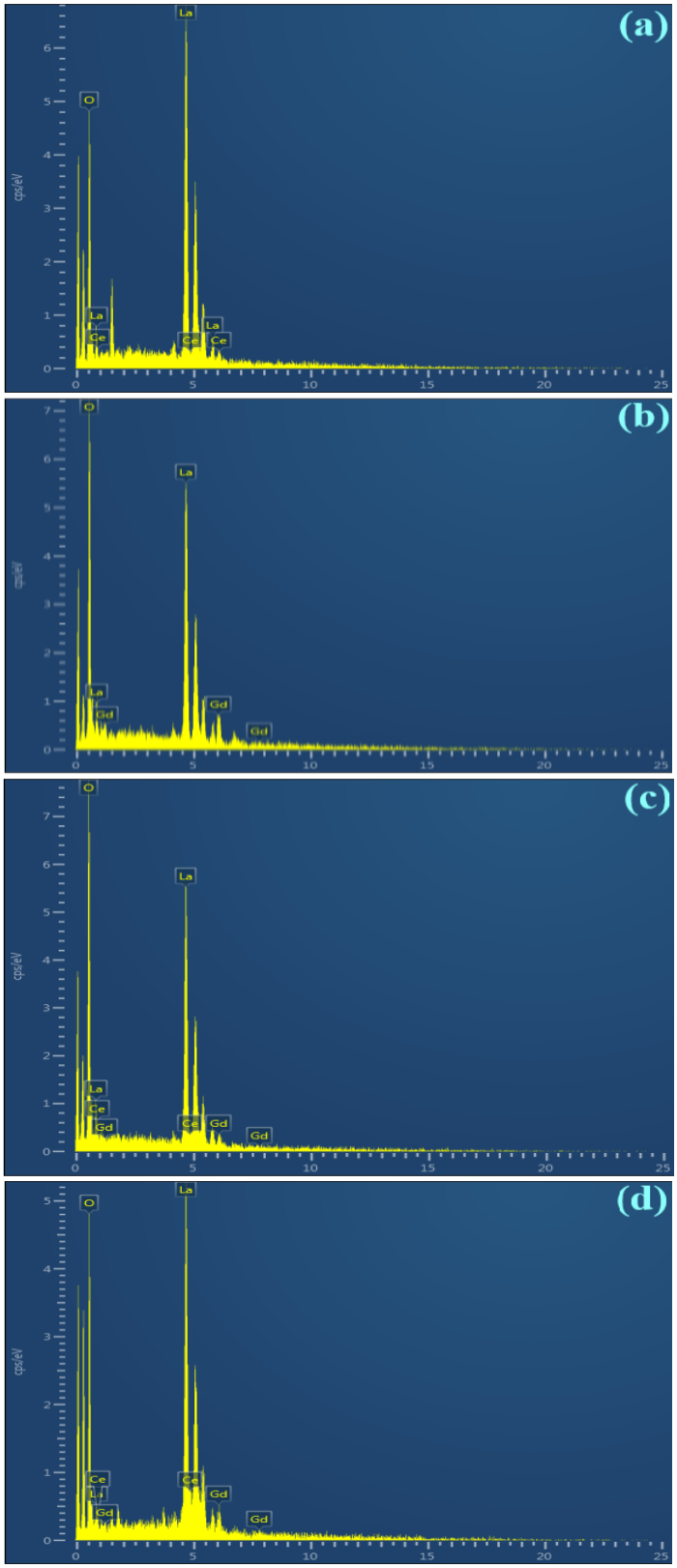
(a)
(b)
(c)
(d)
cps/eV
O
La
Ce
Gd

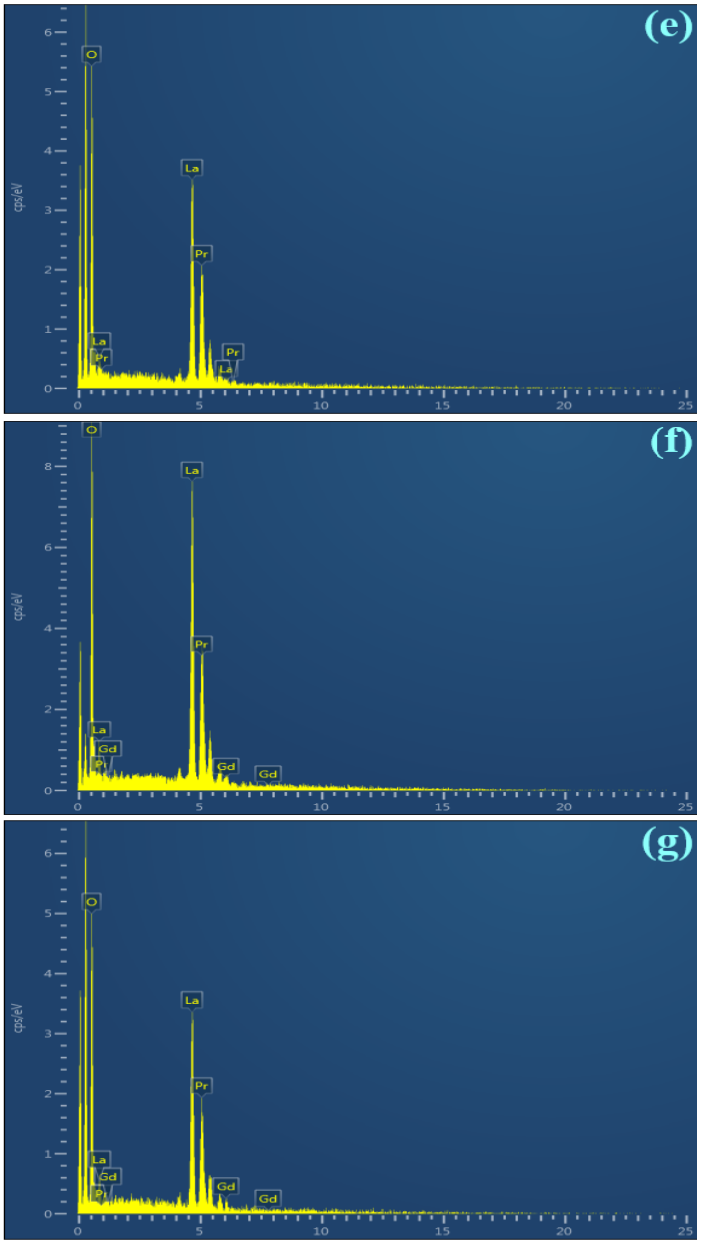

Figure 3.2 EDAX Spectra of Synthesized Samples (a) 1% Ce^{3+}: La_2O_3 (b) 1% Gd^{3+}: La_2O_3 (c) 1% Ce^{3+}, 1% Gd^{3+}: La_2O_3 (d) 2% Ce^{3+}, 1% Gd^{3+}: La_2O_3 (e) 1% Pr^{3+}: La_2O_3 (f) 1% Pr^{3+}, 1% Gd^{3+}: La_2O_3 (g) 2% Pr^{3+}, 1% Gd^{3+}: La_2O_3

Synthesized Materials	Phase Name with Space Group	Matching JCPDS file no.	Avg. Crystallite Size (nm)	Lattice Parameters (A°)			Volume $(A°)^3$
				a	b	c	
1% Ce: La_2O_3	Hexagonal $P\bar{6}2m$	83-1344, 83-1345, 40-1279, 40-1281	21.71	6.267	6.267	3.234	109.86
1% Gd: La_2O_3			22.79				
1% Ce, 1% Gd: La_2O_3			19.63				
2% Ce, 1% Gd: La_2O_3			26.67				
1% Pr: La_2O_3			18.45				
1% Pr, 1% Gd: La_2O_3			28.34				
2% Pr, 1% Gd: La_2O_3			26.01				

Table 3.1 Structural data & lattice parameter of synthesized materials extracted from the XRD spectra

Compounds	Elements (Atomic %)				
	La	O	Ce	Gd	Pr
1% Ce: La_2O_3	30.75	68.35	0.90	-	-
1% Gd: La_2O_3	22.66	77.01	-	0.33	-
1% Ce, 1% Gd: La_2O_3	41.49	57.68	0.32	0.51	-
2% Ce, 1% Gd: La_2O_3	43.03	56.33	0.43	0.21	-

1% Pr: La_2O_3	41.22	58.89	-	-	0.34
1% Pr, 1% Gd: La_2O_3	40.88	58.26	-	0.42	0.44
2% Pr, 1% Gd: La_2O_3	42.34	56.60	-	0.46	0.60

Table 3.2: EDAX data of compounds with weight percentage

Fig. 3.1 shows the XRD pattern of all seven synthesized compounds. The XRD peaks of all compounds are similar. It is clear from the XRD spectrum that doping of rare-earth ions in host La_2O_3 is substitutional and the doping rare earth elements have successfully replaced the La^{3+} ion. The synthesized samples have been found to be in hexagonal phase. The peaks were matched with the JCPDS files No. 83-1344, 83-1345, 40-1279 & 40-1281 of hexagonal La_2O_3 compound. The highest peaks are observed at 2θ values of 15.63° and at 28.02° with hkl values of (100) & (002). The lattice parameters & crystallite size were calculated from the peaks. These are presented in Table 3.1. EDAX spectra estimated the elemental compositions of synthesized samples. Fig. 3.2 (a to g) show the EDAX spectrum of synthesized samples from the EDAX spectra. Peaks for the host as well as the dopant elements can be seen present. As no other elements have been detected, synthesized samples indicate to be having high purity. The spectra indicate appropriate incorporation of the dopants in the host La_2O_3 lattice. Table 3.2 presents the results in terms of atomic percentage.

3.3.2 UV – Visible analysis:

Shimadzu made UV – Visible spectrometer was used to record the absorption spectra. Fig.

3.3 (a to g) shows the absorption characteristics of all synthesized samples. 0.05 M aqueous solutions of samples were used for UV – Visible analysis.

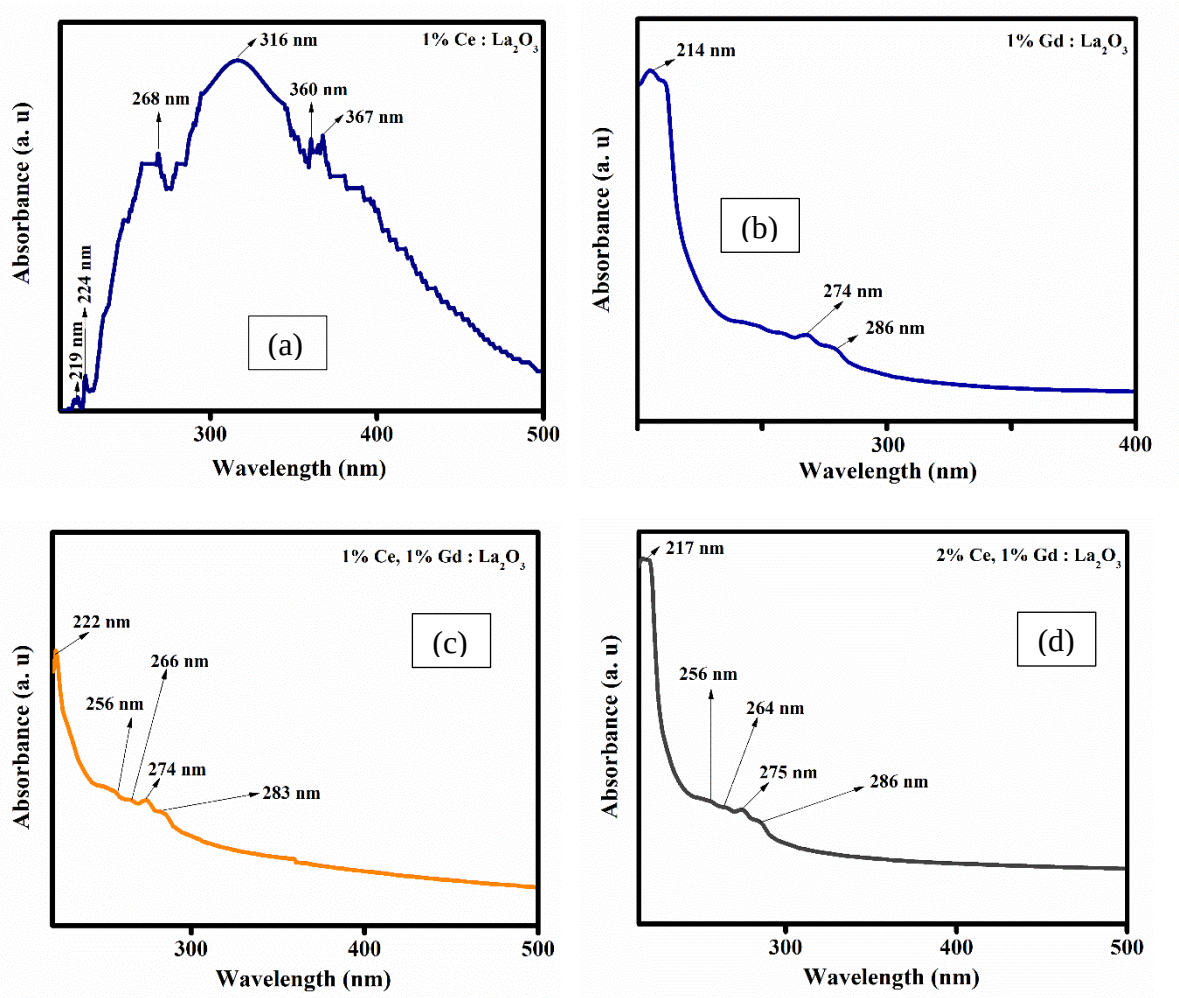

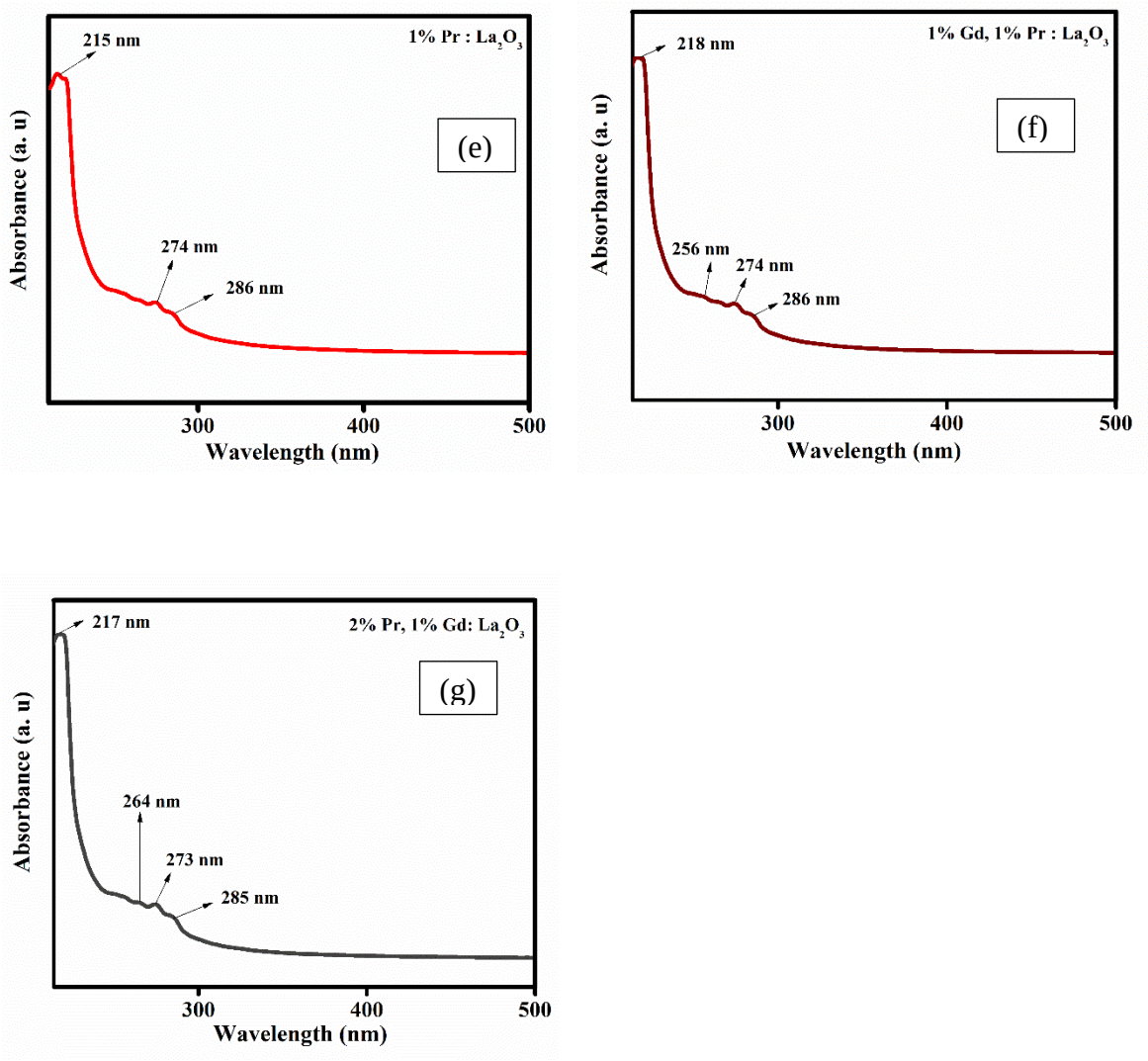

Figure 3.3 UV – Visible Spectra of Synthesized Samples (a) 1% Ce^{3+}: La_2O_3 (b) 1% Gd^{3+}: La_2O_3 (c) 1% Ce^{3+}, 1% Gd^{3+}: La_2O_3 (d) 2% Ce^{3+}, 1% Gd^{3+}: La_2O_3 (e) 1% Pr^{3+}: La_2O_3 (f) 1% Pr^{3+}, 1% Gd^{3+}: La_2O_3 (g) 2% Pr^{3+}, 1% Gd^{3+}: La_2O_3

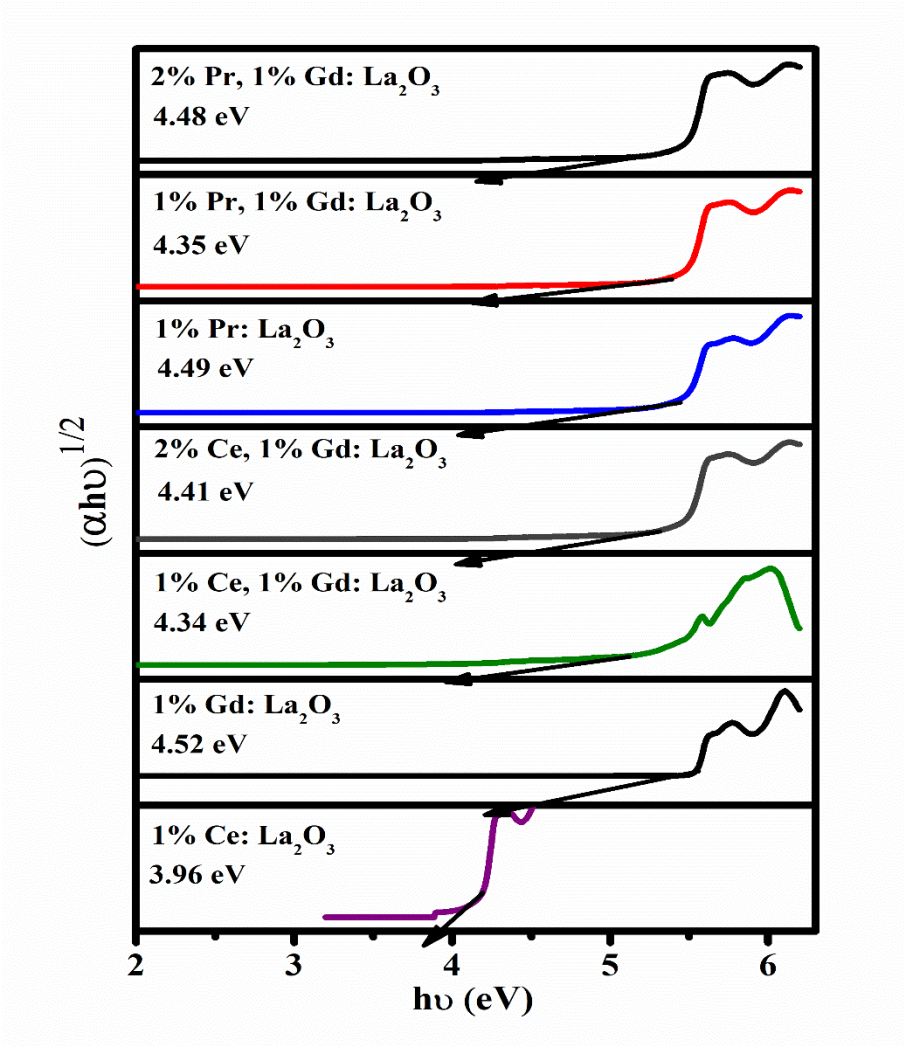

Figure 3.4 Tauc's Plot of Synthesized Samples from UV – Visible Spectra

Compounds	Band Gap (eV)	Refractive index η
1% Ce: La_2O_3	3.96	2.16
1% Gd: La_2O_3	4.52	2.07
1% Ce, 1% Gd: La_2O_3	4.34	2.09
2% Ce, 1% Gd: La_2O_3	4.41	2.08
1% Pr: La_2O_3	4.49	2.07
1% Pr, 1% Gd: La_2O_3	4.35	2.09

2% Pr, 1% Gd: La_2O_3	4.48	2.07

Table 3.3 UV / VIS data of Compounds

Fig. 3.3 (a) showing the absorbance spectra of 1% Ce^{3+}: La_2O_3 displays a maximum at 316 nm, which is attributed to the absorption between 2p orbital of O^{-2} and 5d orbital of Ce^{3+} [39] [40]. The other features observed at wavelengths 367 nm, 360 nm, 268 nm, 224 nm and 219 nm are due to the energy transitions 4f →$5d_1$, 4f→ $5d_2$, 4f →$5d_3$, 4f →$5d_4$ & 4f →$5d_5$ respectively.

In the figures 3.3 (b to g), the absorption around 285 nm is a common feature. Several rare earth dopants do display such absorbance features around the same wavelength, which is due to the absorption between the 2p orbital of O^{-2} and 5d orbital of dopant rare-earth ions.

The highest absorption peak is observed around 215 nm in all samples except the first one i. e. 1% Ce^{3+}: La_2O_3. It is due to the host La_2O_3 absorption. The absorbance spectra of 1% Ce^{3+}: La_2O_3 stands different compared to the other samples, as evident from the spectra. Thus the presence of Ce^{3+} ions looks like inhibiting the host absorption in the given range, the addition of Gd^{3+} ions in other samples as co-activator restore it, indicating the role of Gd^{3+} ions as sensitizer. Other peaks observed in fig. 3.3 (b to g) are likely to be resulting from 4f→5d transition of rare-earth ions.

Fig. 3.4 shows the Tauc plot of all synthesized compounds. The graph is plotted between $(\alpha h\nu)^{1/n} \rightarrow (h\nu)$, which gives the energy bandgap values. Here n = 2 is taken for the allowed indirect electronic transition [41]. The value of bandgap and refractive index [42] for the samples

are given in Table 3.3.

3.3.3 Photoluminescence analysis:

The Photoluminescence excitation and emission spectra were recorded on Shimadzu make spectrophotofluorometer.

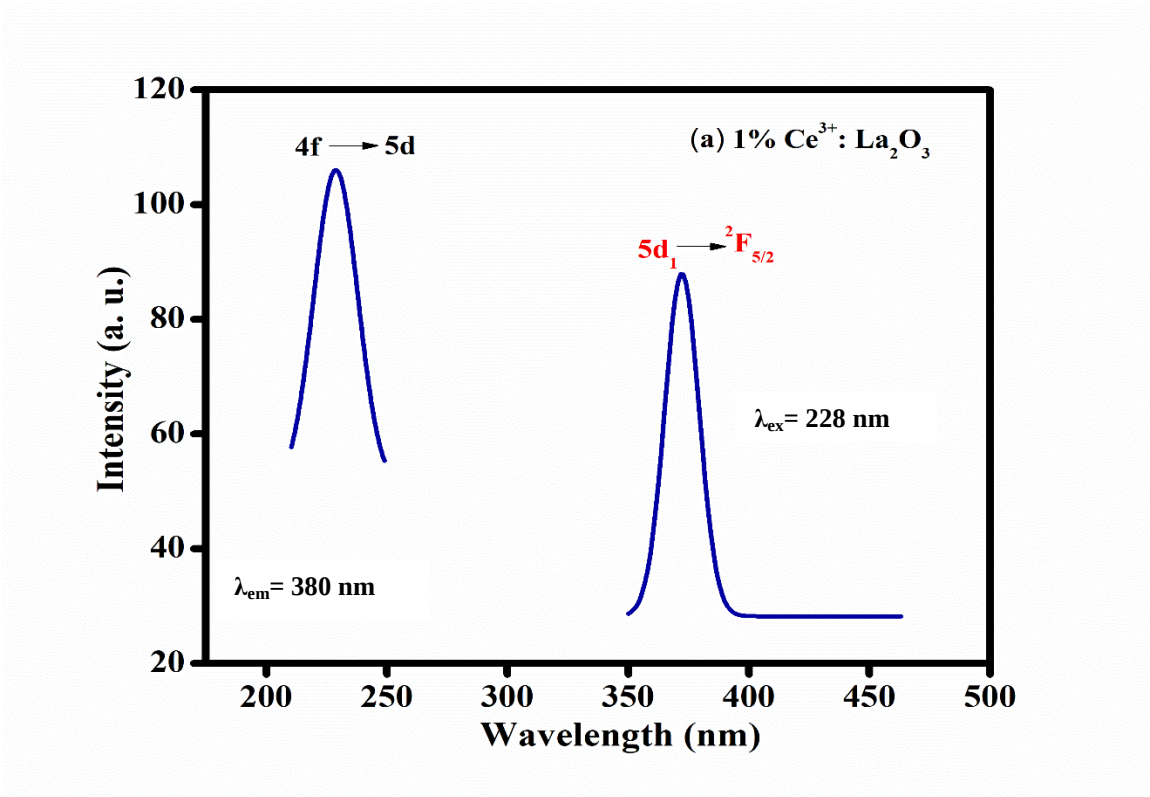

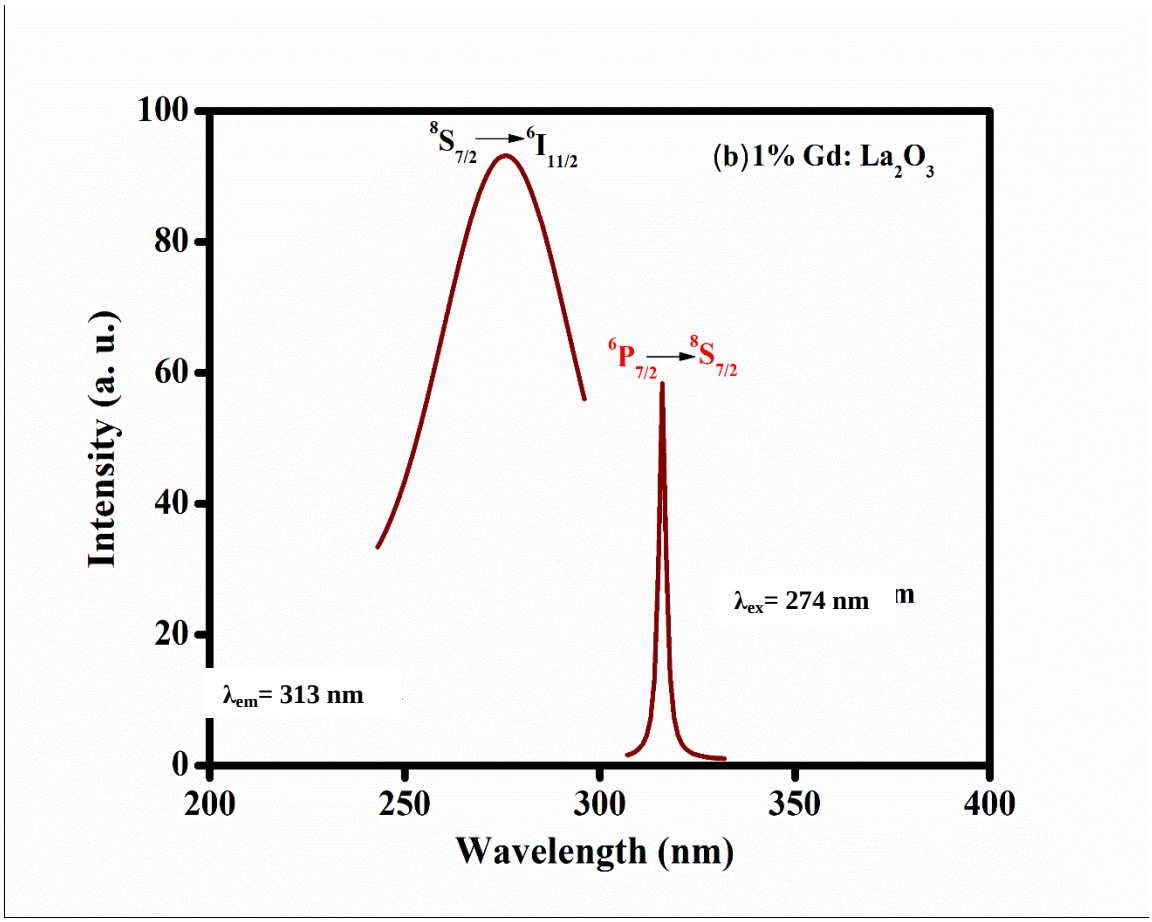
100
80
60
40
20
0
Intensity (a. u.)
200
250
300
350
400
Wavelength (nm)
$^8S_{7/2} \rightarrow {}^6I_{11/2}$
(b)1% Gd: La_2O_3
$^6P_{7/2} \rightarrow {}^8S_{7/2}$
λ_{ex}= 274 nm
λ_{em}= 313 nm

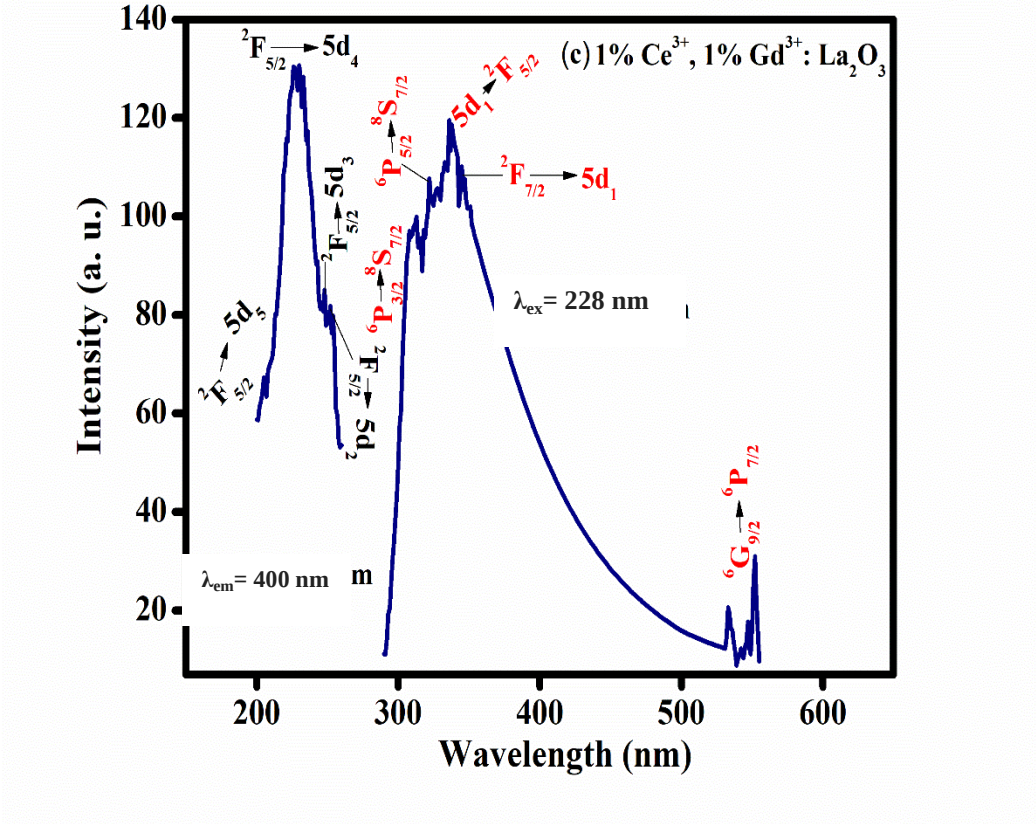
(c) 1% Ce3+, 1% Gd3+: La2O3
2F5/2 → 5d4
2F5/2 → 5d5
2F5/2 → 5d3
2F5/2 → 5d2
6P3/2 8S7/2
6P5/2 8S7/2
5d1 2F5/2
2F7/2 → 5d1
6G9/2 → 6P7/2
λex= 228 nm
λem= 400 nm
Intensity (a. u.)
Wavelength (nm)

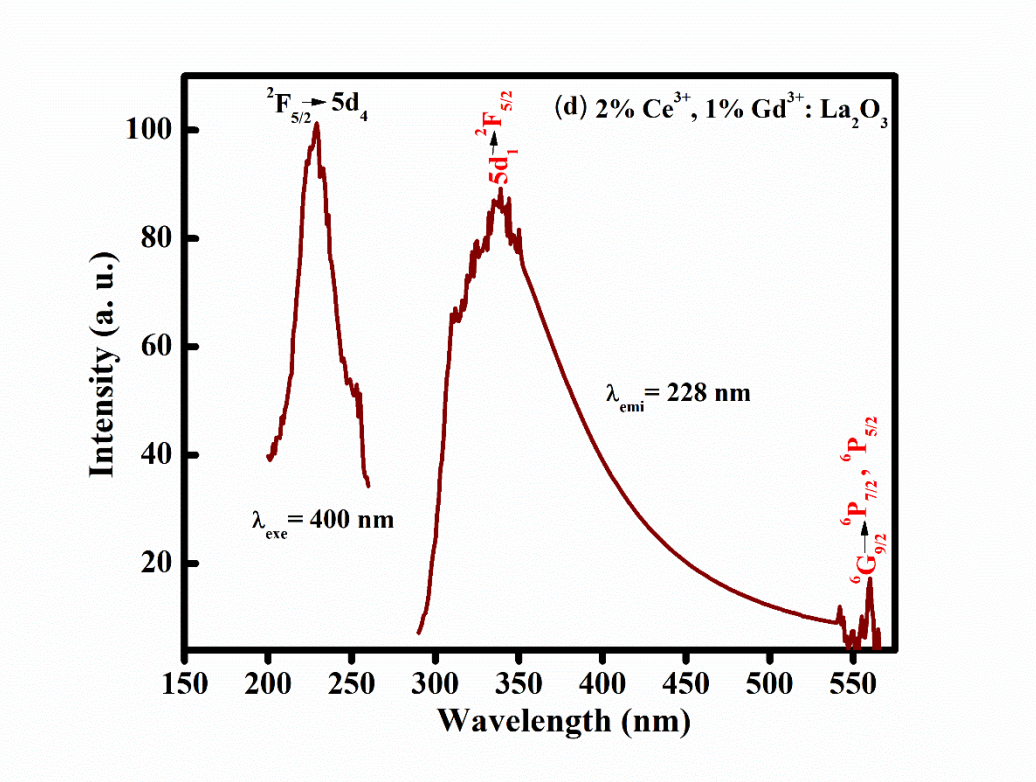
(d) 2% Ce3+, 1% Gd3+: La2O3
2F5/2 → 5d4
2F5/2 → 5d1
λemi= 228 nm
λexe= 400 nm
6G9/2 → 6P7/2, 6P5/2
Intensity (a. u.)
Wavelength (nm)

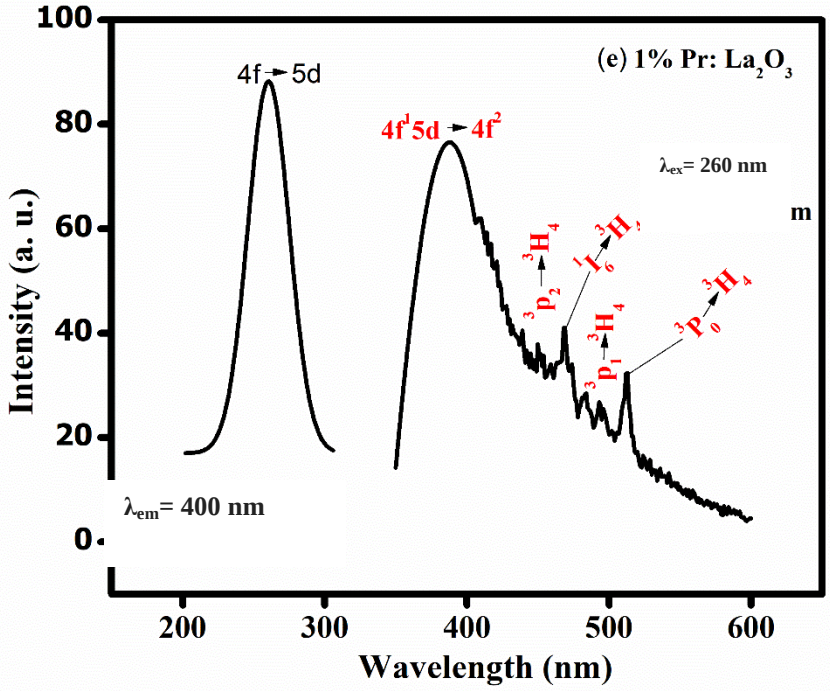
(e) 1% Pr: La2O3
4f → 5d
4f15d → 4f2
λex= 260 nm
λem= 400 nm
Intensity (a. u.)
Wavelength (nm)

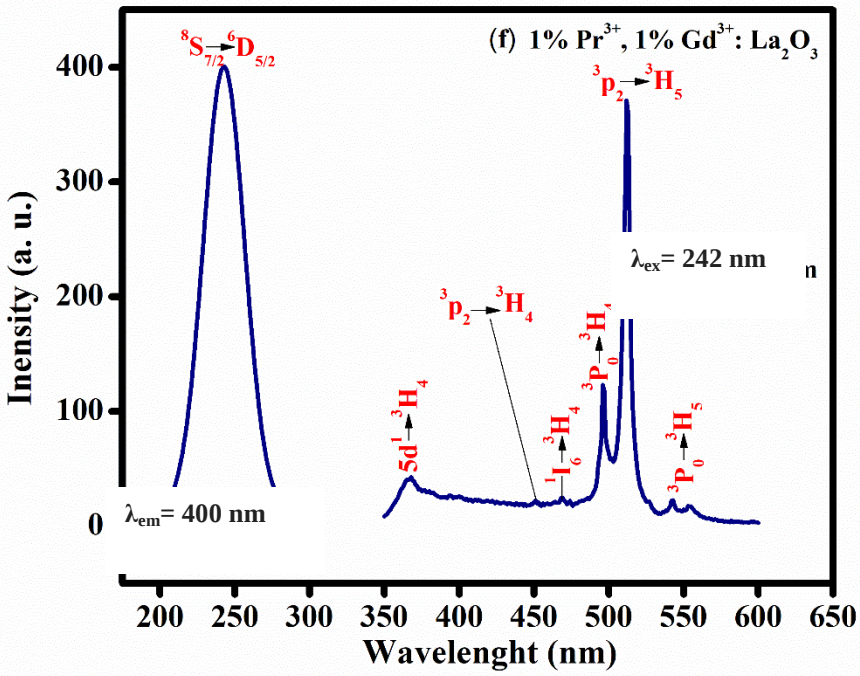
(f) 1% Pr3+, 1% Gd3+: La2O3
8S7/2 → 6D5/2
3p2 → 3H5
λex= 242 nm
3p2 → 3H4
λem= 400 nm
Inensity (a. u.)
Wavelenght (nm)

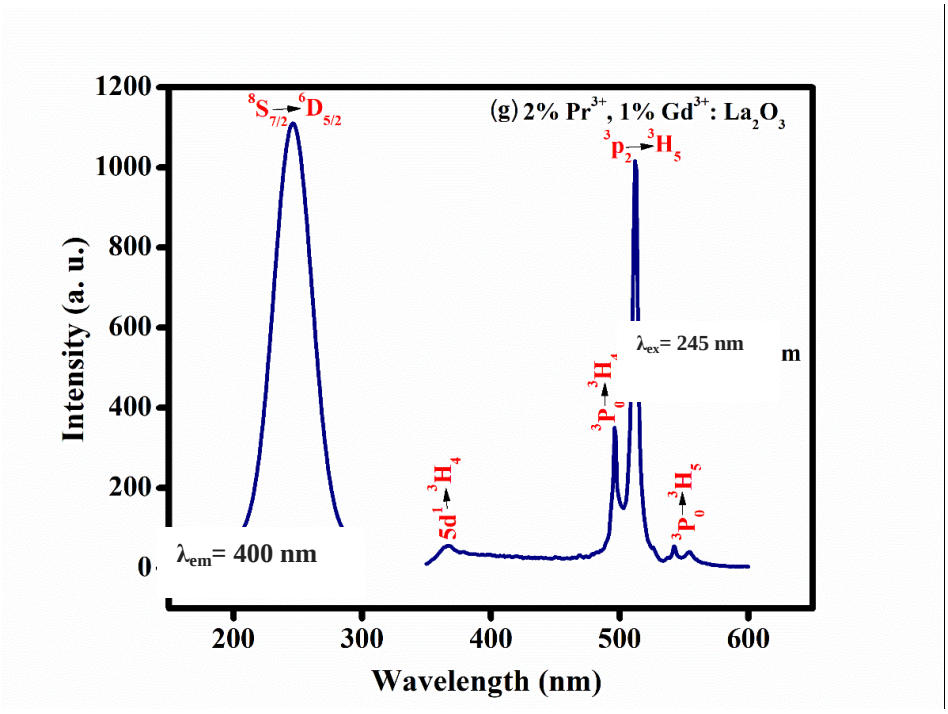

Figure 3.5 PL Excitation & Emission Spectra of Synthesized Samples (a) 1% Ce^{3+}: La_2O_3 (b) 1% Gd^{3+}: La_2O_3 (c) 1% Ce^{3+}, 1% Gd^{3+}: La_2O_3 (d) 2% Ce^{3+}, 1% Gd^{3+}: La_2O_3 (e) 1% Pr^{3+}: La_2O_3 (f) 1% Pr^{3+}, 1% Gd^{3+}: La_2O_3 (g) 2% Pr^{3+}, 1% Gd^{3+}: La_2O_3

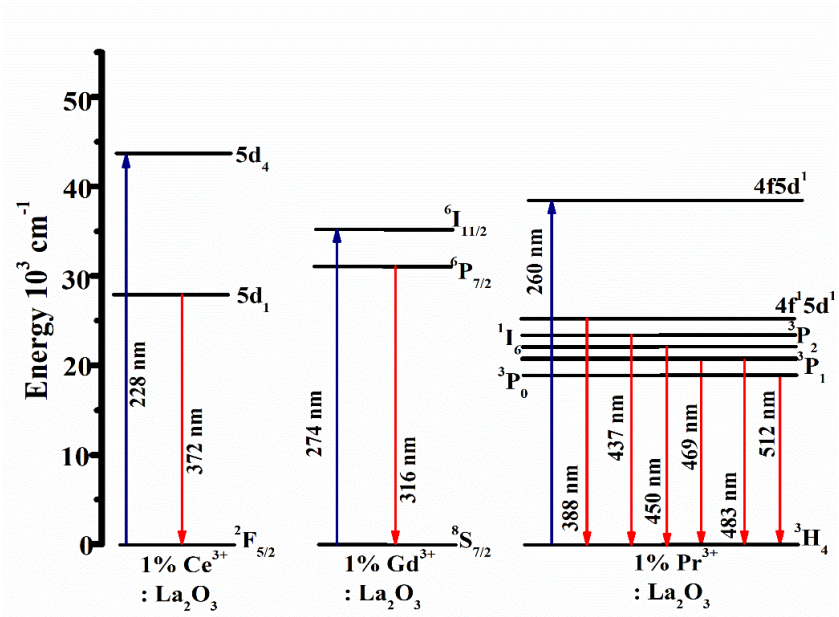

Figure 3.6 (a) Energy transfer process diagrams for PL of rare earth ions in 1% Ce^{3+}:

La_2O_3, 1% Gd^{3+}: La_2O_3 & 1% Pr^{3+}: La_2O_3

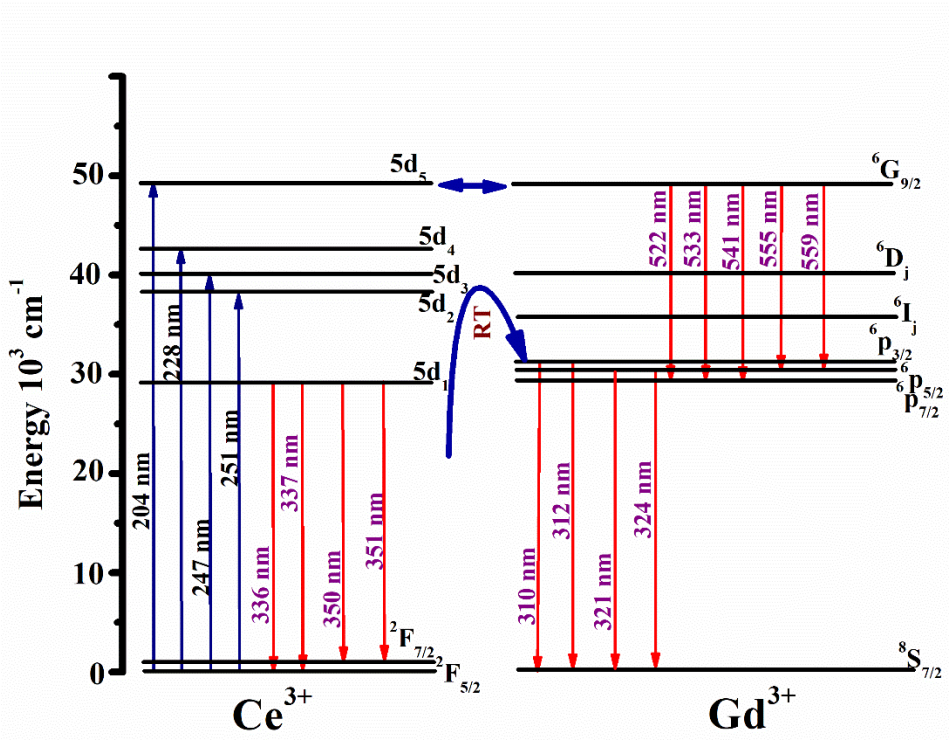

Figure 3.6 (b) Energy transfer process diagrams for PL of rare earth ions in Ce^{3+} - Gd^{3+}: La_2O_3

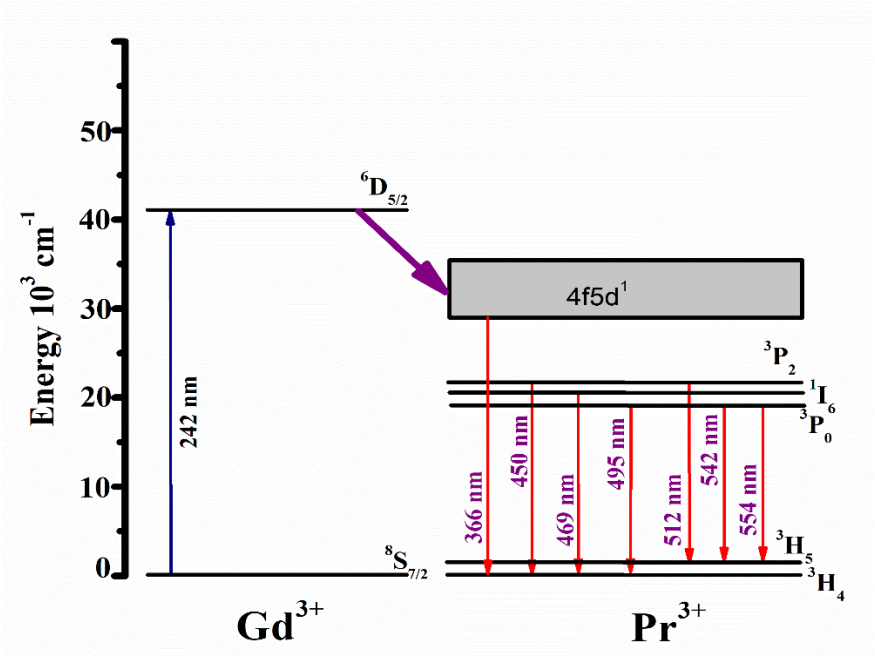

Figure 3.6 (c) Energy transfer process diagrams for PL of rare earth ions in Pr^{3+} - Gd^{3+}:La_2O_3

Compounds	D cm^{-1}	$\mathcal{E}_{cfs}$ cm^{-1}	$\mathcal{E}_c$ cm^{-1}		
			r(1.7)	**r**(2)	**r**(2.4)
1% Ce^{3+}: La_2O_3	22099	18415	13157	14781	16316
1% Ce^{3+}, 1% Gd^{3+}: La_2O_3	19579	19258	10140	11840	13444
2% Ce^{3+}, 1% Gd^{3+}: La_2O_3	19848	19045	10535	12215	13468

Table 3.4 Redshift D, Crystal field splitting $\mathcal{E}_{cfs}$ and Centroid shift $\mathcal{E}_c$ of Synthesized Compounds

The results provide an excellent insight into the mechanisms of energy transfer in rare earth based optical materials. Taking an overview of these mechanisms, they can be categorized into several types.

1) The 4f−5d type in which one of the 4f elect ron(s) is transferred to a 5d orbital.

2) The 4f−4f type in which the electron transfer takes place within the 4f orbitals.

3) The Charge Transfer mechanism in which electrons in the neighboring anions are transferred to a 4f orbital.

The energies of the 4f5d and Charge Transfer transition are more dependent on their environments than the energies of 4f states but the relative order of energies of these states are found to be the same for the whole series of rare earth ions in any host materials.

The emission characteristics i.e. 5d−4f transition also have a correlation with the host crystal

structures in certain cases which affects parameters like quantum yield, emission color, decay rate, thermal quenching, etc. The dielectric constant of the host crystal, geometrical structure of coordination polyhedron around the luminescence center, accurate energies of 4f and 5d levels as well as the position of 4f and 5d levels relative to the valance and conduction bands of the hosts are some other factors that have been given consideration in theoretical calculations.

The 4f−4f5d excitations are often characterized by high radiative emission probability and short lifetime because the f−d transition is electrical dipole allowed. Generally, the f−f transitions result into sharp emission lines. However, the f−d transitions generally give broader excitation and emission features due to high sensitivity of the 5d orbital to the surrounding environment.

The relative and absolute positions of the energy levels of lanthanide Ions assume significance. There are occupied states that can donate electrons and empty states that can accept electrons. There is a downward shift of the lowest-energy 5d level when a lanthanide is brought from the gaseous state (free ion) into the crystalline environment of a compound. Due to the interaction with the neighboring anion ligands (the crystal field interaction), the degenerate 5d levels of the free ion split (crystal field splitting). However, it depends on the site symmetry. In addition, the whole 5d configuration shifts toward lower energy (centroid shift). The crystal field splitting combined with the centroid shift lowers the lowest 5d level with an amount known as the redshift or depression D. The value of D is important as it determines the color of emission and wavelength of absorption of the 4f-5d transitions.

Besides, the quantum efficiency of the luminescence process is of crucial importance as is the thermal stability of the emission in some applications. These aspects are related to the relative and absolute location of the lanthanide energy levels e.g. the position of the host-sensitive lowest

5d state relative to the host-invariant 4f states is important for the quenching behavior of both 5d--4f and 4f-4f emissions by multi phonon relaxation. The absolute position of the 4f and 5d states relative to valence band and conduction band states also affects luminescence quenching and charge-trapping phenomena. Absolute location is crucial for phosphor performance. The experimental and theoretical understanding of the placement of energy levels relative to the intrinsic bands of the host still needs deeper insight.

Since, the study involves a set of dopants/activators/co-activators in the same host, the effect of their incorporation in the host, particularly on the energy levels and their splitting is important. This determines the excitation and emission properties.

It is generally seen that the incorporation of a trivalent lanthanide ion in a host lowers the energy level of the first allowed 4f→4f5d transition of the free trivalent lanthanide. This lowering is measured in terms of the spectroscopic red shift. There are studies which show that the shift remains almost the same for all lanthanides in a given host. The shift is mathematically given as

$$D = \varepsilon c + \frac{\varepsilon cfs}{r} - 1890 \text{ cm}^{-1}$$

In this case, it is a summation of the energy difference between centroid position and lowest 5d level (of free Ce^{3+} ion, which is 1890 cm^{-1}) and the centroid shift. It also depends upon the value of crystal field splitting as well as the ratio of crystal field splitting and crystal field shift. Ce^{3+} has the simplest spectroscopic structure. Studies on the crystal field splitting and crystal field shift of numerous ions suggest that the ratio (r) remains between 1.7 to 2.4. Hence, there values of r, at both extremes and Centre were taken to calculate the values of shifts.

It is with this background that the discussions on the obtained results have been presented.

1) 1% Ce^{3+}: La_2O_3

Fig. 3.5 (a) shows the excitation and emission spectra of 1% Ce^{3+}: La_2O_3. The excitation spectrum was recorded at the emission wavelength λ_{emi} of 380 nm. The excitation spectrum shows only one peak at 228 nm. The emission spectrum recorded at λ_{exc} of 228 nm has the highest peak at 372 nm. The $4f^n \rightarrow 4f^{n-1}$ 5d transitions are mainly responsible for the excitation and emission of Ce^{3+} in the host lattice [13]. The host lattice La_2O_3 also affects the energy difference between the lowest 4f energy level and the first $4f^{n-1}$ 5d energy level of Ce^{3+}, which is determined as redshift D [18]. Generally, redshift is defined as the decrease in the excitation energy of 4f---5d energy level. As mentioned above, the redshift is also a combination of centroid shift ε_c and crystal field splitting ε_{cfs}. The centroid shift of the 5d energy level of lanthanides in the host lattice is observed due to the combined effect of covalency, which is also referred to as the nepheauxetic effect [14] [43] and ligand polarization [43]. The crystal field splitting is also observed in 5d orbitals due to their highly susceptible nature [14]. The 5d orbital of Ce ion is split into five energy levels in La_2O_3 lattice and it is described as $5d_1$, $5d_2$, $5d_3$, $5d_4$ & $5d_5$. This is observed from UV – Visible absorption spectra of 1% Ce^{3+}: La_2O_3. The first absorption is observed at a wavelength of 367 nm (27247 cm^{-1}) from the 4f level to the lowest $5d_1$ level. The subsequent energy levels $5d_2$, $5d_3$, $5d_4$ & $5d_5$ are observed at 360 nm (27777 cm^{-1}), 268 nm (37313 cm^{-1}), 224 nm (44642 cm^{-1}) & 219 nm (45662 cm^{-1}) respectively. As the transition from the valance band to the conduction band is observed at 316 nm (31645 cm^{-1}), the energy levels $5d_3$, $5d_4$ & $5d_5$ are in the conduction band.

The energy value of the splitting of 5d orbital of Ce ion in La_2O_3 is around18415 cm^{-1}($5d_5$ level to $5d_1$ level). So the value of crystal field splitting ε_{cfs} is around 18415 cm^{-1}.

To calculate the redshift D, the following equation [43] is used,

$$E_{abs}\ (La_2O_3) = E_{free} - D\ (La_2O_3) \qquad (1)$$

Here E_{free} is the energy of free Ce ion, which is around 49346 cm^{-1} [13]. The E_{abs} is ascribed to absorption that results into transition from 4f to $5d_1$ energy level and its value is 27247 cm^{-1}. Using this equation, the value of redshift D of Ce^{3+} in La_2O_3 host lattice is obtained, which is around 22099 cm^{-1}. Hence, the decrease in energy between 4f & 5d level is substantial.

The equation [18] used to calculate the approximate values of centroid shift is given by,

$$D = \varepsilon c + \frac{\varepsilon cfs}{r} - 1890 \qquad (2)$$

In this equation, r is termed as the ratio of the crystal field responsible for the redshift. 1890 cm^{-1} is the energy difference between the centroid position and $5d_1$ level of free Ce^{3+} ions. r has a value from 1.7 to 2.4 [18]. For calculation of centroid shift, three values of r i.e. 1.7, 2 & 2.4 have been used here. The approximate values of centroid shifts for these values of r have been found to be ε_{c1} (1.7) = 13157 cm^{-1}, ε_{c2} (2) = 14781 cm^{-1}, ε_{c3} (2.4) = 16316 cm^{-1} respectively.

The excitation maximum is found at 228 nm, which is due to the transition from ground level 4f to $5d^4$energy level. The peak emission wavelength was obtained at 372 nm. The transition from the $5d_1$ level to $^2F_{5/2}$ (ground level of 4f) is responsible for this emission peak. The broadening observed in the spectra is because of 5d to 4f transition.

The emission of 1% Ce^+: La_2O_3 phosphor at the wavelength of 372 nm falls in the UVA region.

2) 1% Gd^{3+}: La_2O_3

The fig. 3.5 (b) shows the excitation and emission spectra of 1% Gd^{3+}: La_2O_3. The free

Gd^{3+} ion has 327 energy levels [13]. The energy levels pertaining to CTS and the $4f^6 5d^1$ states in Gd^{3+} are the highest in comparison with other rare earth materials [13]. $^8S_{7/2}$ is the ground state. One of the energy states of Gd^{3+} ion is located around 50000 cm^{-1} (^6G_j) and many more energy levels are above 50000 cm^{-1} [44]. This is one of the largest energy difference observed amongst the rare earth ions. The excitation spectrum was recorded at λ_{emi} of 313 nm, which has maximum value around the wavelength 274 nm. The excitation at 274 nm is ascribed to $^8S_{7/2} \rightarrow {}^6I_{11/2}$ (36496 cm^{-1}) transition [26]. The emission spectrum recorded at excitation of 274 nm, has a sharp emission line at 316 nm. The electron dipole transition $^6P_{7/2}$ (31645 cm^{-1}) $\rightarrow$ $^8S_{7/2}$ is responsible for this strong emission band. This emission is in the UVB region.

3) 1% Ce^{3+} - 1% Gd^{3+}: La_2O_3

Fig. 3.5 (c) shows the excitation and emission spectra of 1% Ce^{3+} - 1% Gd^{3+}: La_2O_3. The presence of Gd^{3+}ions alter the energy levels of Ce^{3+} ions in the La_2O_3 host compound. The excitation spectrum was recorded at the emission wavelength of 400 nm. The excitation spectrum shows maximum at a wavelength of 228 nm. Sharp features are observed at 204 nm, 247 nm & 251 nm. The 228 nm peak is due to the transition from $^2F_{5/2}$ to $5d_4$ (43859 cm^{-1}). The transitions from $^2F_{5/2} \rightarrow 5d_5$ (49019 cm^{-1}), $^2F_{5/2} \rightarrow 5d_3$ (40485 cm^{-1}) and $^2F_{5/2} \rightarrow 5d_2$ (39840 cm^{-1}) are responsible for the excitation features at wavelengths 204 nm, 247 nm and 251 nm respectively. The emission spectrum was recorded at an excitation wavelength of 228 nm. It is a broadband spectrum with the highest peak at 336 nm. The transition from $5d_1$ (29761 cm^{-1}) to $^2F_{5/2}$ is responsible for this emission peak.

The energy transfers from Ce^{3+} ions to Gd^{3+} ions are proposed to be happening in two ways, Resonance Transfer and Radiative Transfer. The energy transfers from the $5d_5$ level of Ce^{3+} to

the energy level $^6G_{9/2}$ (49019 cm^{-1}) of Gd^{3+} ion is due to resonance transfer. The transfer of energy from Ce^{3+} ions to the $^6P_{3/2}$ energy level of Gd^{3+} ions is due to radiative transfer.

The sharp emission features at wavelengths 312 nm & 321 nm correspond to the energy transitions respectively from $^6P_{3/2}$ (32100 cm^{-1}) to $^8S_{7/2}$ and from $^6P_{5/2}$(31152 cm^{-1}) to $^8S_{7/2}$ of Gd^{3+} ions. The emission at 351 nm is due to the transition from $5d_1$ energy level to $^2F_{7/2}$ (1500 cm^{-1}) of Ce^{3+} ions. These transitions give emission in UV region.

The emission peak at 533 nm is due to the transition from $^6G_{9/2}$ to $^6P_{7/2}$ and at 552 nm is due to transition $^6G_{9/2}$ to $^6P_{5/2}$ respectively.

The parameter like redshift, centroid shift and crystal field splitting of 1% Ce^{3+} - 1% Gd^{3+}: La_2O_3 phosphor is presented in Table 3.4.

4) 2% Ce^{3+} - 1% Gd^{3+}: La_2O_3

As shown in fig. 3.5 (d), the excitation spectrum recorded at a wavelength of λ_{emi} 400 nm has a maximum at 228 nm which is ascribed to $^2F_{5/2}$ to $5d_4$ (43809 cm^{-1}). Sharp features are observed at 204 nm, 247 nm and 252nm. The energy levels of 5d are slightly reduced with increase in the amount of Ce^{3+} ions. The excitation features at wavelengths of 204 nm, 247 nm & 252 nm are due to the transitions from $^2F_{5/2}$ to $5d_5$ (48543 cm^{-1}), $^2F_{5/2}$ to $5d_3$ (40485 cm^{-1}) & $^2F_{5/2}$ to $5d_2$ (39682 cm^{-1}) respectively. The emission spectrum was recorded at an excitation wavelength of 228 nm. The broadening & highest emission peak is observed at a wavelength of 339 nm. The energy transition from $5d_1$ (29498 cm^{-1}) to the ground state $^2F_{5/2}$ is responsible for this emission at 339 nm. Sharp features are observed at 311 nm and 324 nm, which are due to the transitions from $^6P_{3/2}$ (32154 cm^{-1}) to $^8S_{7/2}$ and $^6P_{5/2}$ (31055 cm^{-1}) to $^8S_{7/2}$ respectively of Gd^{3+} ion. Small

emissions peaks are observed in the visible region at wavelength 542 nm, 560 nm due to general transition from $^6G_{9/2}$ to ^6P_j levels of Gd^{3+} ion. The emission peak at 542 nm is due to the transition from $^6G_{9/2}$ to $^6P_{7/2}$ and at 560 nm is due to transition $^6G_{9/2}$ to $^6P_{5/2}$ respectively.

The parameters like redshift, centroid shift and crystal field splitting of 2% Ce^{3+} - 1% Gd^{3+}: La_2O_3 phosphor is presented in Table 3.4.

5) 1% Pr^{3+}: La_2O_3

Fig. 3.5 (e) shows the excitation and emission spectra of 1% Pr^{3+}: La_2O_3. The excitation spectrum was recorded at an emission wavelength of 400 nm. The peak excitation wavelength is at 260 nm (38416 cm^{-1}). The excitation peak is ascribed to $4f \rightarrow 5d^1$ transition for Pr^{3+} ion. This transition depends on the host lattice. The covalence and crystal field of the host lattice environment has a greater effect on the energy level of the 5d shell. The $4f^{n-1}5d^1$ energy level, situated at 38461 cm^{-1} in the excitation spectrum, is the lowest for the Pr^{3+} ion. This energy level is specific to the host, which in this case is La_2O_3.

The emission spectrum was recorded at an excitation wavelength of 260 nm. It is broad band spectra with maximum at 388 nm (25773 cm^{-1}) and sharp features at 437 nm (22883 cm^{-1}), 450 nm (22222 cm^{-1}), 469 nm (21321 cm^{-1}), 483 nm (20703 cm^{-1}), 493 nm (20283 cm^{-1}) and 512 nm (19531 cm^{-1}). The emission at 388 nm is attributed to the transition from $4f^15d^1$ to $^3H_4$, which is an allowed transition and shows broadening. The other six emission lines are weak and ascribed to a $4f^2 \rightarrow 4f^2$ transition. The emissions at the wavelength of 437 nm and 450 nm are due to the transition from $^3P_2$ (22883 cm^{-1}) to $^3H_4$. Emission at wavelengths 483 nm & 493 nm are ascribed to transition from $^3P_1$ (20703 cm^{-1}) to $^3H_4$. The emission at 469 nm and 512 nm is due to transition from $^1I_6$ (21321 cm^{-1}) to $^3H_4$ & from $^3P_0$ (19531 cm^{-1}) to $^3H_4$. Hence, the transition

from $4f^15d^1$ to $4f^2$ is the most dominant emission transition [32].

6) 1% Pr^{3+} - 1% Gd^{3+}: La_2O_3

The fig. 3.5 (f) shows the excitation and emission spectra of 1% Pr^{3+} - 1% Gd^{3+}: La_2O_3. The excitation spectrum was recorded at a wavelength of 400 nm. The excitation band has the highest peak at 242 nm, which is ascribed to a transition from $^8S_{7/2}$ to $^6D_{5/2}$ (41322 cm^{-1}) of Gd^{3+} ion. The excitation energy then transfers to the $4f^15d^1$ state of the Pr^{3+} ion. The presence of Gd^{3+} ion alters the energy level of the 4f5d state of Pr^{3+} ion. The emission spectrum was recorded at an excitation wavelength of 242 nm. There are several emission peaks with the highest emission peak observed at a wavelength of 511 nm due to the transition from $^3P_0$ to $^3H_4$. The small emission peaks observed at 366 nm, 450 nm & 469 nm are ascribed to the transitions $4f5d^1$ to $^3H_4$, $^3P_2$ to $^3H_4$ and $^1I_6$ to $^3H_4$ respectively. The last two emission peaks at wavelengths 542 nm & 554 nm are due to the transition from $^3P_0$ to $^3H_5$ level.

7) 2% Pr^{3+} - 1% Gd^{3+}: La_2O_3

The excitation and emission spectra of 1% Pr^{3+} - 1% Gd^{3+}: La_2O_3 shown in fig. 3.5 (g). The excitation spectrum was recorded at an emission wavelength of 400 nm, which has a maximum excitation peak at 245 nm. This peak is ascribed to the energy transfer from $^8S_{7/2}$ to $^6D_{5/2}$ level of Gd^{3+} ion. The energy is then transferred to the Pr^{3+} ion, which attains 4f5d state. The emission spectrum was recorded at an excitation wavelength of 245 nm. The emissions are observed at 366 nm, 495 nm, 512 nm, 542 nm and 554 nm. The highest peak is observed at 512 nm due to the energy transition from $^3P_0$ to $^3H_4$ level. The transition from $4f5d^1 \rightarrow {}^3H_4$ is responsible for emission at 366 nm, which is a very weak emission. The energy transition from $^3P_0$ to $^3H_5$ level is responsible for the emission of 542 nm & 554 nm. The emission at a wavelength of 495 nm is

ascribed to energy transition from $^3P_1$ to $^3H_4$ energy level.

The emission peaks at a wavelength of 450 nm & 469 nm which were observed in previous sample are not seen in the emission of this sample which has a higher percentage of Pr^{3+} ions.

The 1% Gd^{3+}: La_2O_3 phosphor shows the emission in the UVB region while 1% Ce^{3+}: La_2O_3 & 1% Pr^{3+}: La_2O_3 phosphors show the emission in the UVA region. For Ce – Gd combination, the emission is observed in UVA, UVB & in the visible region. Ce^{3+} ion transfers the energy to Gd^{3+} ion and sensitizes its emission in the visible region and shifts to longer wavelength side in visible region with increasing the concentration of Ce^{3+} ion in Ce^{3+} - Gd^{3+} combination doped La_2O_3 compounds.

The parameters like redshift, crystal field splitting & centroid shift are decreasing compared with 1% Ce^{3+}: La_2O_3. The emission is predominantly in the visible region for the Pr- Gd combination doped La_2O_3 compounds, with a very weak peak observed in the UVA region. Here, the Pr^{3+} ion is sensitized by the Gd^{3+} ion. With increase in the Pr^{3+} ions in the Pr- Gd combination doped La_2O_3 compounds, the intensity of emission rises and a very sharp peak of cyan color is observed.

3.4 Conclusion:

The synthesized compounds have shown emission in UV region and they can be used as UV emitting phosphors. The presence of Gd^{3+} ions alter the energy level of Ce^{3+} ion in Ce^{3+} - Gd^{3+}

combination doped La_2O_3 compounds. In the Pr^{3+} - Gd^{3+} combination doped La_2O_3 compound, the emission is predominantly in the visible region with an intense and sharp peak. It has potential to be used as commercial LED phosphor for cyan color.

References:

[1] I. Ragan, L. Hartson, H. Pidcoke, R. Bowen, R. Goodrich, Pathogen reduction of SARS-CoV-2 virus in plasma and whole blood using riboflavin and UV light, PLoS One. 15 (2020) e0233947. doi:10.1371/journal.pone.0233947.

[2] N. Brownstone, M. Mosca, J. Hong, E. Hadeler, T. Bhutani, Phototherapy for Psoriasis: New Research and Insights, Curr. Dermatol. Rep. (2021). doi:10.1007/s13671-020-00324-z.

[3] H. Stege, K. Ghoreschi, C. Hünefeld, UV phototherapy: UV phototherapy and photodiagnostics—a practical overview, Hautarzt. (2021). doi:10.1007/s00105-020-04744-7.

[4] C.H. Lee, S.B. Wu, C.H. Hong, H.S. Yu, Y.H. Wei, Molecular mechanisms of UV-induced apoptosis and its effects on skin residential cells: The implication in UV-based phototherapy, Int. J. Mol. Sci. (2013). doi:10.3390/ijms14036414.

[5] P. Sahu, V.K. Jain, K. Aggarwal, S. Kaur, S. Dayal, Tacalcitol: a useful adjunct to narrow-band ultraviolet-B phototherapy in vitiligo, Photodermatol. Photoimmunol. Photomed. (2016). doi:10.1111/phpp.12265.

[6] A. Takada, K. Matsushita, S. Horioka, Y. Furuichi, Y. Sumi, Bactericidal effects of 310 nm ultraviolet light-emitting diode irradiation on oral bacteria, BMC Oral Health. (2017). doi:10.1186/s12903-017-0382-5.

[7] R. K.P., F. M.E., A. K.L., F. S.R., A Review of the Use of Tanning Beds as a

Dermatological Treatment, Dermatol. Ther. (Heidelb). (2015).

[8] A. Gabet, H. Métivier, C. de Brauer, G. Mailhot, M. Brigante, Hydrogen peroxide and persulfate activation using UVA-UVB radiation: Degradation of estrogenic compounds and application in sewage treatment plant waters, J. Hazard. Mater. (2021). doi:10.1016/j.jhazmat.2020.124693.

[9] A. Nguyen, D. Krupke, M. Burbage, S. Bhatnagar, S.P. Fekete, A.T. Becker, Using a UAV for Destructive Surveys of Mosquito Population, in: Proc. - IEEE Int. Conf. Robot. Autom., 2018. doi:10.1109/ICRA.2018.8463184.

[10] C. Zhou, C. Jiang, J. Zhao, P. Zhan, X. Tang, D. Jin, X. Wang, Bi3+-doped Ba2Y1−xLuxNbO6:Bi3+ (0 ≤ x ≤ 1.0) solid solution phosphors: tunable photoluminescence and application for white LEDs, Bull. Mater. Sci. (2021). doi:10.1007/s12034-020-02307-z.

[11] L. Gariazzo, G. Gasparini, A. Casabella, L. Carmisciano, A. Clapasson, F. Murgioni, L. Molfetta, E. Cozzani, A. Parodi, Is ultraviolet radiation avoidance affecting bone health in melanoma patients?, Photodermatol. Photoimmunol. Photomed. (2021). doi:10.1111/phpp.12657.

[12] H. Luo, L. Zhong, Ultraviolet germicidal irradiation (UVGI) for in-duct airborne bioaerosol disinfection: Review and analysis of design factors, Build. Environ. (2021). doi:10.1016/j.buildenv.2021.107852.

[13] G.H. Dieke, H.M. Crosswhite, B. Dunn, Emission Spectra of the Doubly and Triply Ionized Rare Earths*, J. Opt. Soc. Am. 51 (1961) 820. doi:10.1364/josa.51.000820.

[14] X. Qin, X. Liu, W. Huang, M. Bettinelli, X. Liu, Lanthanide-Activated Phosphors Based on 4f-5d Optical Transitions: Theoretical and Experimental Aspects, Chem. Rev. 117

(2017) 4488–4527. doi:10.1021/acs.chemrev.6b00691.

[15] L. Wu, B. Liu, J. Zhang, B. Han, A novel UV-emitting Ce 3+ -doped chloroborate Ba 2 GaB 4 O 9 Cl phosphor, Optik (Stuttg). 184 (2019) 241–246. doi:10.1016/j.ijleo.2019.03.064.

[16] Z. Zhang, J. Liang, L. Sun, S. Wang, Q. Sun, B. Devakumar, S. Rtimi, X. Huang, Synthesis and photoluminescence properties of near-UV-excitable cyan-emitting Ca2YHf2Ga3O12:Ce3+ garnet phosphors, J. Lumin. 227 (2020) 117544. doi:10.1016/j.jlumin.2020.117544.

[17] P. Dorenbos, T. Shalapska, G. Stryganyuk, A. Gektin, A. Voloshinovskii, Spectroscopy and energy level location of the trivalent lanthanides in LiYP4O12, J. Lumin. 131 (2011) 633–639. doi:10.1016/j.jlumin.2010.11.005.

[18] P. Dorenbos, (formula presented)-level energies of (formula presented) and the crystalline environment. III. Oxides containing ionic complexes, Phys. Rev. B - Condens. Matter Mater. Phys. 64 (2001) 1–12. doi:10.1103/PhysRevB.64.125117.

[19] I. Milisavljevic, Y. Wu, E. Zych, The effect of Gd3+ doping on luminescence properties of (Gd, Ce): SrF2 nanopowders and transparent ceramics, J. Lumin. 224 (2020) 117243. doi:10.1016/j.jlumin.2020.117243.

[20] I. Adell, R.M. Solé, M.C. Pujol, M. Lancry, N. Ollier, M. Aguiló, F. Díaz, Single crystal growth, optical absorption and luminescence properties under VUV-UV synchrotron excitation of type III Ce3+:KGd(PO3)4, a promising scintillator material, Sci. Rep. 8 (2018) 1–11. doi:10.1038/s41598-018-29372-z.

[21] ENERGY TRANSFER PHENOMENA IN Li(Y, Gd)F4: Ce, Th H.S. KILIAAN*, A. MEIJERINK and G. BLASSE, 35 (1986) 155–161.

[22] H. Suzuki, T.A. Tombrello, C.L. Melcher, J.S. Schweitzer, Energy transfer from Gd to Ce in Gd2(SiO4)O : Ce, J. Lumin. 60–61 (1994) 963–966. doi:10.1016/0022-2313(94)90321-2.

[23] S.C. Gedam, Optical study of Gd 3 + and Tb 3 + in KZnSO 4 Cl : Ce 3 + Phosphor, 1 (2013) 6–10.

[24] X. Cao, S. Sun, B. Lu, Y. Liu, R. Ma, H. Cao, H. Ma, H. Huang, Spectral photoluminescence properties of YAG: Ce, R (R: Gd3+, Pr3+, Gd3+ and Pr3+) transparent fluorescent thin film prepared by pulse laser deposition, J. Lumin. 223 (2020) 117222. doi:10.1016/j.jlumin.2020.117222.

[25] N. Singh, J.K. Lee, M. Mohapatra, R.M. Kadam, V. Singh, UV emitting Gd incorporated LiBaB9O15 phosphors: An ESR and photoluminescence investigation, J. Lumin. 223 (2020) 117239. doi:10.1016/j.jlumin.2020.117239.

[26] V. Singh, B.R. Venkateswara Rao, A.S. Rao, J.L. Rao, M. Irfan, Photoluminescence and electron spin resonance study on narrow-band UVB emitting Gd-doped LaPO4 phosphors, Optik (Stuttg). 206 (2020) 164020. doi:10.1016/j.ijleo.2019.164020.

[27] D. Shuang, T. Wanjun, X. Guangyong, Y. Yuhong, H. Zhengxi, Synthesis and photoluminescence tuning of (Sr,Ln)9Mg1.5(PO4)7 phosphors by Ln (Ln = Y, La, Gd, Lu) substitution, J. Lumin. 224 (2020) 1–6. doi:10.1016/j.jlumin.2020.117331.

[28] R.G. Kunghatkar, P.S. Hemne, S.J. Dhoble, UVB emitting LiSrBO3phosphor for phototherapy lamp, AIP Conf. Proc. 1953 (2018) 3–8. doi:10.1063/1.5032844.

[29] J.A. Jiménez, Silicon-Induced UV Transparency in Phosphate Glasses and Its Application to the Enhancement of the UV Type B Emission of Gd3+, ACS Appl. Mater. Interfaces. 9 (2017) 15599–15604. doi:10.1021/acsami.7b03162.

[30] D.S. Thakare, S.K. Omanwar, P.L. Muthal, S.M. Dhopte, V.K. Kondawar, S. V. Moharil, UV-emitting phosphors: Synthesis, photoluminescence and applications, Phys. Status Solidi Appl. Res. 201 (2004) 574–581. doi:10.1002/pssa.200306720.

[31] Z. Tian, H. Liang, B. Han, Q. Su, Y. Tao, G. Zhang, Y. Fu, Photon cascade emission of Gd3+ in Na(Y,Gd)FPO4, J. Phys. Chem. C. 112 (2008) 12524–12529. doi:10.1021/jp802975g.

[32] Z. Yang, J.H. Lin, M.Z. Su, Y. Tao, W. Wang, Photon cascade luminescence of Gd3+ in GdBaB9O16, J. Alloys Compd. 308 (2000) 94–97. doi:10.1016/S0925-8388(00)00908-7.

[33] B.P. Gangwar, S. Irusta, S. Sharma, Physicochemical and optical properties of one-pot combustion synthesized Pr doped La2O3/La(OH)3, J. Lumin. 219 (2020). doi:10.1016/j.jlumin.2019.116893.

[34] Y. Shimizu, Y. Takano, K. Ueda, UV emissions in Gd3 + doped or Gd3 +-Pr3 + Co-doped III-III perovskite-type RMO3 (R = Y, La; M = Al, Ga), Thin Solid Films. 559 (2014) 23–26. doi:10.1016/j.tsf.2013.11.135.

[35] G. Blasse, J.P.M.V.A.N. Vliet, J.W.M. Verwey, R. Hoogendam, M. Wiegel, Blasse G. et al. Luminescence of Pr3+ in scandium borate (ScBo3) and the host lattice dependence of the stokes shift //Journal of Physics and Chemistry of Solids. – 1989. – T. 50. – №. 6. – C. 583-585., 50 (1989) 583–585.

[36] T. Jiang, B. Du, H. Zhang, D. Yu, L. Sun, G. Zhao, C. Yang, Y. Sun, M. Yu, M.N.R. Ashfold, High-performance photoluminescence-based oxygen sensing with Pr-modified ZnO nanofibers, Appl. Surf. Sci. 483 (2019) 922–928. doi:10.1016/j.apsusc.2019.04.053.

[37] I. Carrasco, K. Bartosiewicz, F. Piccinelli, M. Nikl, M. Bettinelli, Structural effects and

5d→4f emission transition shifts induced by Y co-doping in Pr-doped K3Lu1−xYx(PO4)2, J. Lumin. 189 (2017) 113–119. doi:10.1016/j.jlumin.2016.08.022.

[38] J. Ueda, A. Meijerink, P. Dorenbos, A.J.J. Bos, S. Tanabe, Thermal ionization and thermally activated crossover quenching processes for 5d-4f luminescence in Y3 A l5-x G ax O12: P r3+, Phys. Rev. B. 95 (2017) 1–8. doi:10.1103/PhysRevB.95.014303.

[39] S. Imashuku, K. Wagatsuma, Cathodoluminescence Analysis of Nonmetallic Inclusions in Steel Deoxidized and Desulfurized by Rare-Earth Metals (La, Ce, Nd), Metall. Mater. Trans. B Process Metall. Mater. Process. Sci. (2020). doi:10.1007/s11663-019-01732-8.

[40] J. Ma, M. Fang, N.T. Lau, On the synergism between La2O2S and CoS2 in the reduction of SO2 to elemental sulfur by CO, J. Catal. (1996). doi:10.1006/jcat.1996.0024.

[41] J. Tauc, R. Grigorovici, A. Vancu, Optical Properties and Electronic Structure of Amorphous Germanium, Phys. Status Solidi. (1966). doi:10.1002/pssb.19660150224.

[42] V. Kumar, J.K. Singh, Model for calculating the refractive index of different materials, Indian J. Pure Appl. Phys. (2010).

[43] P. Dorenbos, The 4fn↔4fn-1 5d transitions of the trivalent lanthanides in halogenides and chalcogenides, J. Lumin. 91 (2000) 91–106. doi:10.1016/S0022-2313(00)00197-6.

[44] S.P. Feofilov, Y. Zhou, H.J. Seo, J.Y. Jeong, D.A. Keszler, R.S. Meltzer, Host sensitization of Gd3+ ions in yttrium and scandium borates and phosphates: Application to quantum cutting, Phys. Rev. B - Condens. Matter Mater. Phys. 74 (2006)1-9.doi:10.1103/PhysRevB.74.085101.